EFFECT OF BLENDING ON HIGH-PRESSURE LAMINAR FLAME SPEED MEASUREMENTS, MARKSTEIN LENGTHS, AND FLAME STABILITY OF HYDROCARBONS

A Thesis

by

WILLIAM BAUGH LOWRY

Submitted to the Office of Graduate Studies of
Texas A&M University
in partial fulfillment of the requirements for the degree of

MASTER OF SCIENCE

December 2010

Major Subject: Mechanical Engineering

Effect of Blending on High-Pressure Laminar Flame Speed Measurements, Markstein Lengths, and Flame Stability of Hydrocarbons

EFFECT OF BLENDING ON HIGH-PRESSURE LAMINAR FLAME SPEED MEASUREMENTS, MARKSTEIN LENGTHS, AND FLAME STABILITY OF HYDROCARBONS

A Thesis

by

WILLIAM BAUGH LOWRY

Submitted to the Office of Graduate Studies of
Texas A&M University
in partial fulfillment of the requirements for the degree of

MASTER OF SCIENCE

Approved by:

Chair of Committee,	Eric L. Petersen
Committee Members,	Timothy J. Jacobs
	M. Sam Mannan
Head of Department,	Dennis O'Neal

December 2010

Major Subject: Mechanical Engineering

ABSTRACT

Effect of Blending on High-Pressure Laminar Flame Speed Measurements, Markstein Lengths, and Flame Stability of Hydrocarbons.

(December 2010)

William Baugh Lowry, B.S., Texas A&M University

Chair of Advisory Committee: Dr. Eric L. Petersen

Natural gas is the primary fuel used in industrial gas turbines for power generation. Hydrocarbon blends of methane, ethane, and propane make up a large portion of natural gas and it has been shown that dimethyl ether can be used as a supplement or in its pure form for gas turbine combustion. Because of this, a fundamental understanding of the physical characteristics such as the laminar flame speed is necessary, especially at elevated pressures to have the most relevance to the gas turbine industry. This thesis discusses the equations governing premixed laminar flames, historical methods used to measure the laminar flame speed, the experimental device used in this study, the procedure for converting the measured data into the flame speed, the results of the measurements, and a discussion of the results. The results presented in this thesis include the flame speeds for binary blends of methane, ethane, propane, and dimethyl ether performed at elevated pressures, up to 10-atm initial pressure, using a spherically expanding flame in a constant-volume vessel. Also included in this thesis is a comparison between the experimental measurements and four chemical kinetic models. The C4 mechanism, developed in part through collaboration between the National University of Ireland Galway and Texas A&M, was improved using the data presented herein, showing good agreement for all cases. The effect of blending ethane, propane, and dimethyl ether with methane in binary form is emphasized in this study, with the resulting Markstein length, Lewis number (Le), and flame stability characterized and discussed. It was noticed in this study, as well as in other studies, that the critical radius of the flame typically decreased as the Le decreased, and that the critical radius of the flame increased as the Le increased. Also, a rigorous

uncertainty analysis has been performed, showing a range of 0.3 cm/s to 3.5 cm/s depending on equivalence ratio and initial pressure.

ACKNOWLEDGMENTS

I would first like to acknowledge my advisor, Dr. Petersen, for his incredible work ethic, pleasant attitude, and availability to his students, setting a high benchmark for everyone that works with and for him. I feel that this work would not have been as achievable without his guidance. Thanks also go out to my committee members, Dr. Jacobs and Dr. Mannan, for serving on my committee and providing helpful insight.

I would also like to thank my immediate co-workers, former and present, for the help they have provided in this work. I thank Jaap deVries for designing the current experimental apparatus, with his foresight allowing our method to have many advantages over previous attempts at this research. I also thank Michael Krecji for his work in helping to perform experiments and for helpful discussions while trying to analyze some of our results. Finally, I also thank the rest of my co-workers at the lab for helping to make work something to look forward to and a fun place.

I would like to thank my wife for her patience while working on this research, particularly during last summer's travel before our wedding and shortly after getting married. I finally thank my Mom and Dad for their encouragement and for pushing me when I didn't want to be pushed, knowing what was best for me when I didn't want it. Thank you for teaching me what hard work means and how to do it.

NOMENCLATURE

Abbreviations

c_p	Specific heat (KJ/kg-K)
$D_{i,j}$	Diffusivity of species *i* into *j* (m^2/s)
h	Specific enthalpy (KJ/kg)
Le	Lewis Number
$\dot{m}$"	Mass burning rate per unit area (kg/m^2-s)
M_w	Molecular weight (kg/kmol)
X	Mole fraction (kmol/kmol)
Y	Mass fraction (kg/kg)

Subscripts

b	Burned condition
i	For species i
L	Laminar flame
u	Unburned condition

Superscripts

o	Un-stretched condition

Greek Symbols

λ	Thermal conductivity (W/m-K)
ρ	Density (kg/m^3)
$S_{L,b}$	Burned, stretched laminar flame speed
$S_{L,b}^o$	Burned, un-stretched laminar flame speed

$S_{L,u}^{o}$	Unburned, un-stretched laminar flame speed
$\vec{v}$	Velocity (m/s)
$v_{i,diff}$	Diffusion velocity for species *i* (m/s)
$\dot{\omega}_i$	Molar production rate for species *i* (kmol/m^3-s)

TABLE OF CONTENTS

Page

Page

LIST OF FIGURES

Page

Page

LIST OF TABLES

CHAPTER I

INTRODUCTION

The laminar premixed flame speed is a fundamental physical property of a combustible mixture related to the mixture composition, stoichiometry, temperature, and pressure (Bradley et al., 1998). For gas turbine combustion systems, the laminar flame speed of a premixed combustible mixture is important for predicting combustion phenomena such as flash back, blow off, and dynamic instabilities (Bourque et al., 2008; Lieuwen and Yang, 2005).

The laminar flame speed of reference fuels such as methane, ethane, propane, and dimethyl ether (DME) have been studied at atmospheric pressure extensively in the past using multiple methods. The methodologies used include the stagnation flame (Vagelopoulos and Egolfopoulos, 1998; Zhao et al., 2004), Bunsen burner (Gibbs and Calcote, 1959; Natarajan et al., 2007), heat flux method (Bosschaart and de Goey, 2004; Konnov et al., 2003; Dyakov et al., 2007; Van Maaren and de Goey, 1994), and outwardly propagating spherical flame (Aung et al., 1995; Hassan et al., 1998a, 1998b; Gu et al., 2000; Rozenchan et al., 2002; Tahtouh et al., 2009; Metghalchi and Keck, 1980; Law and Kwon, 2004; Qin and Ju, 2005; Huang et al., 2007; Chen et al., 2009; de Vries et al., 2010; Daly et al., 2001; Chen et al., 2007). There is a need, however, to determine the laminar flame speed of these fuels at engine-relevant conditions, but studies providing such data are scarce (Jomaas et al., 2005; Gu et al., 2000; Rozenchan et al., 2002).

Additionally, it has been shown that natural gas composition varies dramatically with location and season. In fact, the methane composition of natural gas can vary between 55.8% and 98.1%, ethane can vary between 0.5% and 13.3%, and propane can vary between 0% and 23.7% (Liss et al., 1992). This variation of fuel composition could present significant operation problems for land-based gas turbines because of the variation in the flame speed for these fuels, especially at engine conditions. Previous research has been

---

This thesis follows the style of *Combustion Science and Technology*.

done on methane mixed with various higher order hydrocarbons (Bourque et al., 2008), but this study focuses on binary blends of methane, ethane, propane, and DME. In addition to its practical necessity, the study of fuel blends provides a good fundamental test for the validation of chemical kinetics models.

As mentioned above, real fuel like natural gas is a multi-species mixture with greatly varying proportions. For a chemical kinetics mechanism to be comprehensive and reliable, it must be validated against a large body of data, not only for pure species but also for mixtures. The laminar flame speed of a combustible mixture is an important target for chemical kinetics mechanisms, so testing the flame speed of pure fuel species and fuel mixtures is essential. Also, there are few chemical kinetics models that accurately predict laminar flame speed in addition to high-temperature shock-tube and low-temperature rapid compression machine (RCM) ignition properties for pure and binary blended fuels. The C4 kinetic model, developed in part through collaboration between Texas A&M and The National University of Ireland Galway, has been verified for C1-C4 alkanes at high pressure for pure fuels and their blends for laminar flame speed and high-temperature shock-tube and low-temperature RCM ignition target data (Lowry et al., 2010a; Petersen et al., 2007; Healy et al., 2008a, 2008b), for the laminar flame speed of pure DME at elevated pressures (de Vries et al., 2010), and for other hydrocarbons (Healy et al., 2010a, 2010b; O'Conaire et al., 2004). In the present study, the improved version of the C4 kinetic model is presented, and the model performs well for all experimental conditions tested.

Combustion-bomb, spherical flame speed measurements yield important and practical results, namely the unstretched laminar flame speed and Markstein length. The former can be used for chemical kinetic validation, whereas the latter is a measure of the flame response to stretch. The Markstein length is used to calculate the Markstein number, a parameter that is utilized to predict flame stability. In the context of a real combustion system, the Markstein number is an indicator of the propensity of a system to be influenced by thermo-acoustic instability (Aldredge and Killingsworth, 2004). Stretch is also observed to influence emissions of NOx and CO (Sung and Law, 1998).

The final goal of this thesis was to investigate the effect of blending on the Markstein length and flame stability. In this thesis, a flame is considered stable as long as it can be characterized as a laminar flame. It is therefore unstable if the flame is no longer laminar, and this can be visualized by first implementing the residual method presented herein and then confirmed by observing the flame surface roughness in the recorded images. The dynamics of these types of flame instabilities are coupled with the Lewis number (Law, 1988), and the role of the Lewis number on flame stability has been investigated since Manton et al. (1951). It was the conclusion of Manton et al. (1951) that thermal diffusive processes affected flame stability because if the instabilities were caused solely by hydrodynamic effects, then the equivalence ratio would have no effect on the flame stability. However, it was seen that different fuels displayed varying stabilities, and a connection between the thermal and mass diffusivity was made. It has also been experimentally shown by Rozenchan et al. (2002) that using helium in place of nitrogen as the diluent provided increased flame stability due to the increased flame thickness, which helped to control hydrodynamic instabilities, and the increased mixture Lewis number, controlling thermal-diffusive instabilities. One way to isolate the cause of the instabilities is to alter the mixture Lewis number without greatly changing the flame thickness. To do this, binary blends of fuels that display opposite trends in Lewis number have been made such that thermal-diffusive instabilities should be affected, but the flame thickness should not change by a large amount. These blends have been tested experimentally, and the trends in their Lewis number and critical flame radii have been evaluated.

This thesis is divided by chapters. In Chapter II, the background of laminar premixed flames is discussed, including the equations that govern a premixed flame, chemical kinetic modeling, measurement techniques employed by previous researchers, and the theory behind flame front instabilities. Chapter III covers the experimental apparatus used for taking the flame speed measurements in detail, including the gas handling manifold, pressure vessel, and optical system. Data analysis is covered in Chapter IV, detailing the method used to turn the flame radii and time steps into the unburned, unstretched flame speed. The uncertainty analysis is also discussed in Chapter IV, showing the influence of each parameter's uncertainty on the

experimental measurement. Chapter V presents the results and discusses the trends seen in the data, correlating the critical radii and Lewis numbers. Finally, Chapter VI concludes this thesis.

CHAPTER II

BACKGROUND

2.1 Premixed Laminar Flame Theory

The definition of a flame, taken from Turns (2000), is a self-sustaining propagation of a localized combustion zone at subsonic velocities. In this definition, two important things are discussed. First, a flame is localized, meaning that the reaction does not uniformly occur throughout the combustible mixture, but only occupies a small portion of the mixture at any point in time. Second, a flame in this context is traveling at a subsonic velocity and is therefore a deflagration.

Premixed flames can be described by dividing the flame into two zones, the preheat zone and the reaction zone. Figure 1 gives an example of this division, including the temperature and fuel mass fraction profile across the flame thickness, δ.

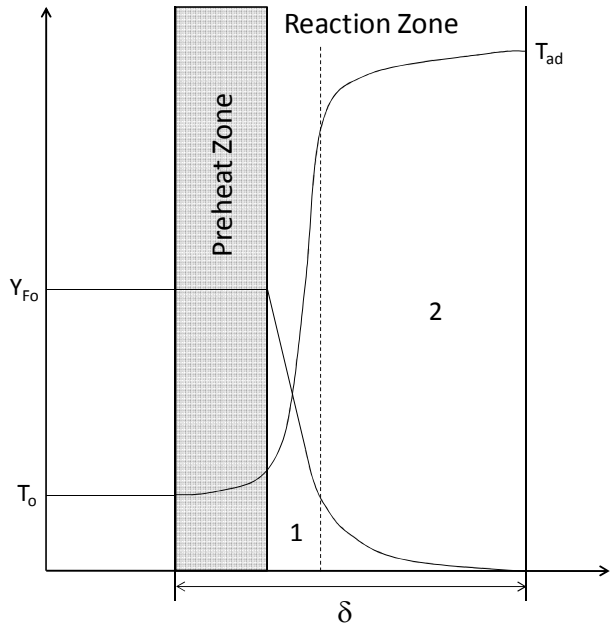

Figure 1 Temperature and fuel species profile across a flame.

In the preheat zone of a flame, the temperature of the reactants is increased by heat flux from the reaction zone. The preheat zone does not have much heat release as the majority of the reactions occur in the reaction zone that follows. The reaction zone can be further broken into two distinct sections. The first section of the reaction zone, denoted by 1 in Figure 1, is a thin region of fast chemistry. This section is dominated by bimolecular reactions and is where the fuel molecules are quickly broken down, and many intermediate species are formed. The secondary reaction zone, illustrated by 2 in Figure 1 is dominated by three-body radical recombination reactions, which are much slower (Turns, 2000). This zone is much thicker than the fast chemistry section. Figure 2 gives a sketch of a one-dimensional, steady, planar flame with the reference frame fixed to the flame.

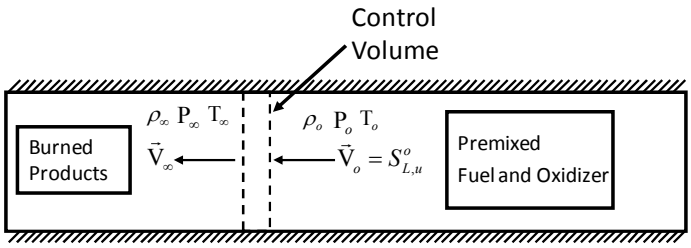

Figure 2 Control volume analysis for a steady, one-dimensional, planar flame.

The conditions before and after the flame are shown in Figure 2, with the unburned state shown to the right of the control volume and the burned state shown to the left of the control volume. The equations governing the propagation of a premixed laminar flame are mass conservation, species conservation, and energy conservation. Due to the fact that deflagrations are essentially constant pressure, the momentum equation does not govern them. The following development was taken from Turns (2000).

Key assumptions for this analysis are:

1. One-dimensional, steady flow.
2. Kinetic and potential energies, viscous shear work, and thermal radiation are all neglected.
3. Pressure is constant.

Conservation of Mass

The conservation of mass equation reduces to Eq. (1) for one-dimensional, steady flow.

$$\frac{d\dot{m}''}{dx} = 0 \;\rightarrow\; \rho_o v_o = \rho_\infty v_\infty \tag{1}$$

In Eq. (1), ρ_o is the unburned density, v_o is the unburned velocity, ρ_∞ is the burned density, and v_∞ is the burned velocity.

Conservation of Species

The conservation of species is slightly more complex, including the change in species mass fraction, diffusion, and volumetric species production, shown in Eq. (2).

$$\dot{m}'' \frac{dY_i}{dx} + \frac{d}{dx}\left(\rho Y_i v_{i,diff}\right) = \dot{\omega}_i M_w \tag{2}$$

Here, $\dot{m}''$ is the mass burning rate per unit area, Y_i is the mass fraction of species *i*, ρ is the density of the mixture, $v_{i,diff}$ is the diffusion velocity of species *i*, $\dot{\omega}_i$ is the volumetric species production rate, and M_w is the molecular weight of the mixture.

Conservation of Energy

The conservation of energy equation considers energy change due to chemical reactions, boundary conditions, and diffusion. The simplified equation for the assumptions listed is given by Eq. (3).

$$\dot{m}'' c_p \frac{dT}{dx} + \frac{d}{dx}\left(-k\frac{dT}{dx}\right) + \sum_{i=1}^{N} \rho\, Y_i v_{i,diff} c_{p,i} \frac{dT}{dx} = -\sum_{i=1}^{N} h_i \dot{\omega}_i M_w \tag{3}$$

In Eq. (3), c_p is the mixture specific heat, k is the thermal conductivity of the mixture, $c_{p,i}$ is the specific heat of the species *i*, and h_i is the enthalpy of species *i.* To solve these three equations and predict the laminar flame speed of a combustible mixture, numerical programs are typically used. In this study, the Premix module in Chemkin (CHEMKIN-PRO, 2008) was used to solve the equations. Additionally, the following relations or data are required and implemented using the numerical solver:

1. Idea gas equation of state.
2. Relations for diffusion velocities.

3. Temperature dependent species properties.
4. Mixture property relations.
5. Chemical kinetic mechanism for $\dot{\omega}_i$'s.
6. Boundary Conditions

The input for the numerical solver includes a detailed chemical kinetic mechanism, the thermodynamic properties for all of the molecules contained in the kinetic mechanism, and the transport properties for the molecules. The diffusion parameters, temperature-dependent species properties, and the mixture property relations are calculated using the input data provided by the user. The chemical kinetic mechanism includes the molecules of interest for the combustion system under study, the reactions considered for the system, and different inputs for the reaction rate coefficients. The two most common reaction rate inputs follow either the solely temperature-dependent form, or a form that includes the effects of pressure on the reaction. The reaction rate in the forward direction for the solely temperature-dependent reactions are given by Eq. (4).

$$k_f = AT^B exp\left[\frac{-E_a}{\bar{R}T}\right] \quad \textbf{(4)}$$

Here, A is the pre-exponential temperature factor, B is a temperature dependency factor, $\bar{R}$ is the universal gas constant, T is the temperature, and E_a is the activation energy. In Eq. (4), k_f is the forward reaction rate for a given reaction. For a pressure-dependent reaction, the Troe formulation (Troe, 1983) is used for the mechanism herein. Figure 3 gives an illustration of a pressure-dependent rate coefficient as a function of pressure.

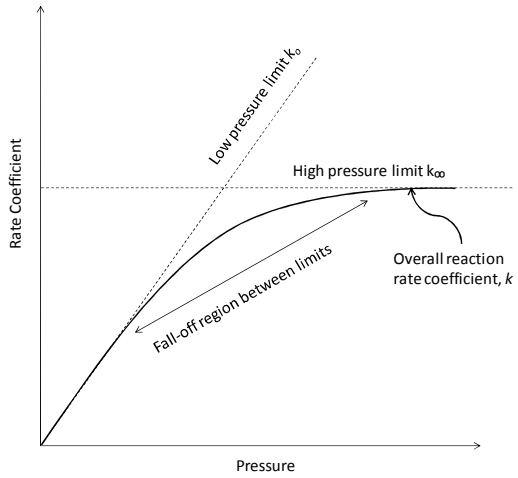

Figure 3 High- and low-pressure limits for pressure dependent reactions.

As shown in Figure 3, the low-pressure limit for the rate coefficient is a function of pressure, while the high-pressure limit is not a function of pressure. The rate coefficients for the low- and high-pressure limits are given by k_o and k_∞, respectively, and can be expressed in Arrhenius form shown in Eqs. (5-6).

$$k_o = A_o T^{B_o} exp\left[\frac{-E_{a,o}}{\bar{R}T}\right] \quad \textbf{(5)}$$

$$k_\infty = A_\infty T^{B_\infty} exp\left[\frac{-E_{a,\infty}}{\bar{R}T}\right] \quad \textbf{(6)}$$

The overall reaction rate coefficient, k, can be found by applying Eqs. (7-13).

$$k = k_f \frac{Pr}{1+Pr} F \quad \textbf{(7)}$$

$$Pr = \frac{k_o[M]}{k_\infty} \quad \textbf{(8)}$$

$$log10(F) = \frac{log10(Fc)}{1+\left\{\frac{log10(Pr)+c}{N-d(log10(Pr)+c)}\right\}^2} \quad \textbf{(9)}$$

$$c = -0.4 - 0.67 log10(Fc) \quad \textbf{(10)}$$

$$N = 0.75 - 1.27 log10(Fc) \quad \textbf{(11)}$$

$$d = 0.14 \quad \textbf{(12)}$$

$$Fc = (1-a)\exp\left(\frac{-T}{T^{***}}\right) + a\exp\left(\frac{-T}{T^{*}}\right) + \exp\left(\frac{-T^{**}}{T}\right) \quad \textbf{(13)}$$

In summary, for the solely temperature-dependent reactions, the reaction rate inputs for the kinetics file are *A, B,* and *Ea*. For the pressure dependent reactions, the inputs include A_o, B_o, $E_{a,o}$, A_∞, B_∞, $E_{a,\infty}$, as well as the fitting parameters a, T^*, T^{**}, and T^{***}. A sample kinetics file is given in the Appendix to illustrate the parameters discussed above. As an example of how the kinetics and the three governing equations are connected, consider a simple reaction with reactants going to products, as in Eq. (14).

$$A + B \rightleftarrows C + D \tag{14}$$

The rate of change of species *A* or *B* in the forward direction is given by Eq. (15), and this provides the input to Eqs. (2-3).

$$\dot{\omega}_A = \dot{\omega}_B = \frac{d[A]}{dt} = \frac{d[B]}{dt} = -k_f[A][B] \tag{15}$$

The final parameters needed to solve the above relations are the boundary conditions for the flame. For the conservation of energy equation, two conditions in T are needed. Equations 16 and 17 provide the needed boundary conditions for conservation of energy.

$$T(x \to -\infty) = T_u \tag{16}$$

$$\frac{dT}{dx}(x \to +\infty) = 0 \tag{17}$$

For the species conservation equation, two boundary equations for Y_i are needed and are given by Eqs. (18-19).

$$Y_i(x \to -\infty) = Y_{i,o} \tag{18}$$

$$\frac{dY_i}{dx}(x \to +\infty) = 0 \tag{19}$$

The final boundary condition, Eq. (20), fixes the coordinate system to move with the flame by specifying the temperature at a fixed location, and this constraint gives the needed information to solve the continuity equation.

$$T(x_1) = T_1 \tag{20}$$

In this study, four kinetic mechanisms are compared to the experimentally measured laminar flame speed. Three of the mechanisms, GRI 3.0 (Smith et al., 1999), JetSurF (Egolfopoulos et al., 2009), and San Diego (San Diego, 2005) are compared in the form available from the respective websites. The fourth mechanism, Curran's C4 mechanism (Petersen et al., 2007), was adjusted through collaboration with the

National University of Ireland Galway to get better agreement with the present data. The kinetic model adjustments are further detailed in the Chemical Kinetic Modeling section.

2.2 Measurement Techniques

Various methods have been used to measure the laminar flame speed. These methods include Bunsen burners, burner stabilized flames, stagnation flames, and outwardly propagating spherical flames. These methods will be described in detail in the following sections.

Bunsen Burner

The Bunsen burner technique was used as one of the first ways to measure the laminar flame speed by Badin, Stuart, and Pease (1949), Clingman, Brokaw, and Pease (1953), and Gibbs and Calcote (1959). It is a method that is easy to set up and is very economical, depending on the complexity of the system used. The apparatus used typically consists of a calibrated gas handling system to adjust the equivalence ratio and gas velocity, a mixing section to ensure a premixed system, a burner, and an optic system to capture the flame images. Early systems used shadowgraph techniques and film cameras, while newer studies using the Bunsen burner method incorporate chemiluminescense and high-speed digital photography (Natarajan et al., 2007). To calculate the laminar burning velocity, the volumetric flow rate is measured, and the burned area of the flame is calculated from the flame images. Equation 21 gives the relation between flame speed, volumetric flow rate, and burned flame area.

$$S_u \approx \frac{\dot{Q}}{A_b} \tag{21}$$

In Eq. (21), the flame speed is not truly the unstretched laminar flame speed, due to curvature effects on the conical flame (Law, 2006). However, the technique of Natarajan et al. (2007) using chemiluminescense greatly improves the accuracy of this approach by selecting the reaction zone as the burned area, compared to using the whole flame with a shadowgraph or schlieren method. This has been shown to agree more closely with the unburned, unstretched laminar flame speed results of researchers

using other methods. Figure 4 is an example image from Natarajan et al. (2007), showing the luminous reaction zone as the area used in Eq. (21).

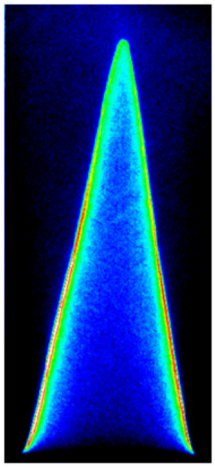

Figure 4 Luminous zone using chemiluminescence on Bunsen burner flame (Natarjan et al. 2007).

Flat Flames

Similar to Bunsen burner flames, flat flames are developed using a burner plate. However, for the flat flames, the burner plate is specifically designed so that flame does not exit the burner in a conical manner, but ideally exits as a flat flame. This situation appears to approach the unstretched, unburned laminar flame desired, but there are non-ideal effects when implementing this method in the laboratory. In this case, the planar flame is stabilized through heat loss to the surface of the burner, resulting in a non-adiabatic flame. The flame becomes adiabatic only when there is zero heat loss to the burner and the flame becomes unstable. There are different variations on this measurement technique, including the heat flux method, and the single jet-wall stagnation method. These techniques are discussed in the following sections.

Heat Flux Method

In the heat flux method, the heat loss required for flame stabilization is balanced by the convective heat flux from the burner surface to the flame front. This type of measurement technique has been used by Van Maaren and de Goey (1994), Dyakov et al. (2001), Konnov et al. (2003), Bosschaart and de Goey (2004),

and Dyakov et al. (2007). Balancing the heat loss and heat gain is done by heating the burner head using 353-K water, cooling the plenum with 298-K water, and monitoring the temperature of the burner head using thermocouples. The experimental apparatus used by Dyakov et al. (2001) is shown in Figure 5.

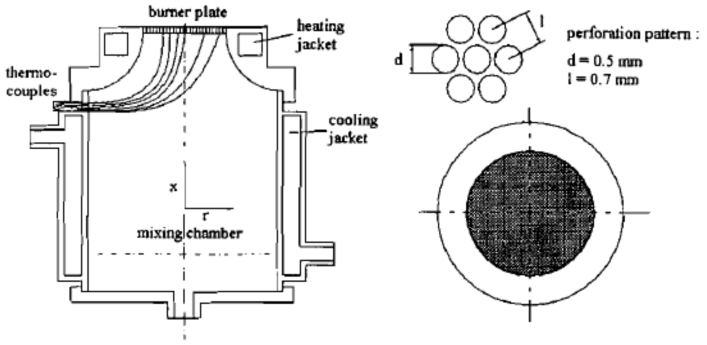

Figure 5 Heat flux experimental apparatus used by Dyakov et al. (2001).

The theory is that the sum of the heat gain from the heating jacket and the heat loss from the cooling jacket should sum to zero when the gas velocity is at the adiabatic burning velocity. If the sum of heat loss and heat gain is higher than zero, then the gas velocity is slower than the adiabatic burning velocity. Similarly, if the sum of the heat loss and heat gain is less than zero, then the gas velocity is faster than the adiabatic velocity. Additionally, when the gas is flowing at the adiabatic burning velocity, the temperature of the burner head is uniform and equal to the temperature of the heating jacket. This measurement technique is not without limitations however, as only flow velocities below 50 cm/s can be measured (Bosschaart and de Goey, 2004), and high-pressure measurements are difficult.

Single Jet-Wall Stagnation

The single jet-wall stagnation method uses a jet emerging from a nozzle impinging on a plate to create a stagnation flow field. As the flow leaves the nozzle, it transitions from a negatively stretched flame to a positively stretched flame. At low flow velocities and large separation distances between the stagnation plate and nozzle, the flame stabilizes as a negatively stretched Bunsen burner flame. However, as either the separation distance is decreased or the flow velocity is increased, the flame transitions to a positively stretched stagnation flame. It is evident that at some point, the flame transitions from a negatively

stretched flame, through a region of near-zero strain rate, and then into a positively stretched flame. The largest benefit of this measurement method is that it allows direct measurement of low strain rate flames. However, the flames are not without stretch affects. Additionally, depending on the Lewis number, rich or lean measurements are not possible with this method. Thermodiffusive instabilities, discussed in Chapter 2.3, were present for mixtures near Le < 1 (Vagelopoulos and Egolfopoulos, 1998). Therefore, appropriate changes in diluent are necessary to stabilize these near-limit flames. Figure 6, from Vagelopoulos and Egolfopoulos (1998), shows the transition from a negatively stretched flame to a positively stretched flame.

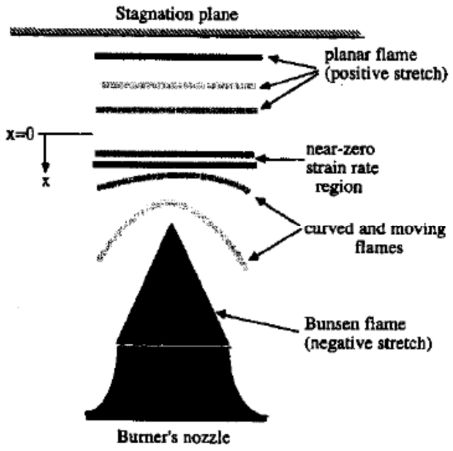

Figure 6 Transition from a negatively stretched flame to a positively stretched flame (Vagelopoulos and Egolfopoulos, 1998).

In Vagelopoulos and Egolfopoulos (1998), it was stated that the separation-distance-to-nozzle-diameter ratio should be between 1.5 and 2.5 ($1.5 < L/D < 2.5$) to establish both a stagnation flame and a Bunsen-type flame. In practice, the transition through the near-zero strain rate region is achieved by establishing the positively stretched stagnation flame and then decreasing the flow velocity and allowing the flame to transition to the Bunsen type flame. Laser Doppler velocimetry (LDV) measurements are made during this process to measure the velocity of the low-stretch flame. The unstretched, unburned laminar flame speed is defined as the minimum local velocity measured as the nozzle exit velocity is decreased. This technique has been used by a number of investigators, including Vagelopoulos and Egolfopoulos (1998) and Zhou et al. (2004).

Outwardly Propagating Spherical Flame

The previously discussed measurement methods require flowing gases to perform the experiments, resulting in substantial uncertainties in the equivalence ratio due to the inherent uncertainties in determining mass flow rates. This imprecision, in turn, results in large uncertainties for the lean and rich flames where a small change in equivalence ratio results in a large change in the laminar flame speed. Instead, it is possible to measure the flame speed using an outwardly propagating spherical flame through stationary gases inside of a closed vessel. There are two ways to measure the laminar flame speed using a constant-volume combustion chamber. The first and more classical method uses the pressure and temperature history to calculate the flame speed through thermodynamic relations, as done by Metghalchi and Keck (1980). The second method uses optical observation of the flame as a function of time to resolve the laminar burning velocity. The latter is used in this study and is preferred due to the ability to visualize the flame and any corresponding instabilities on the surface of the flame that may accelerate the flame speed.

The optically observed, outwardly propagating spherical flame has been used extensively in the past to measure the laminar flame speed of combustible mixtures. A short list of investigators using this method include Aung et al. (1997), Hassan et al. (1998a & b), Gu et al. (2000), Rozenchan et al. (2002), Law and Kwon (2004), Jomaas et al. (2005), de Vries (2009), and Tahtouh et al. (2009). This technique begins with making a combustible mixture using the partial pressure method. After the gases have been allowed to become fully mixed, they are ignited across electrodes, and the propagation of the flame is visualized as a function of time. The radius and time values measured from the flame front history are then used to find the unburned, unstretched laminar flame speed after data analysis. The method used to analyze the data is covered in the Data Analysis section.

2.3 Flame Instabilities

In explaining flame instabilities, two possible causes have been identified. The two things thought to cause flame instabilities are 1) hydrodynamic instabilities and 2) diffusion instabilities. The next two sections present the theory behind each.

Hydrodynamic Instabilities

Hydrodynamic instabilities were first investigated by Landau (1944) and Darrieus (1938). Both investigators have similar theories behind the causes of hydrodynamic instabilities. In Figure 7, reprinted from Manton et al. (1951), the principle of hydrodynamic instability is visualized. According to this theory, after a ripple is formed on the surface of a flame, it will grow until limited by the process of wave propagation.

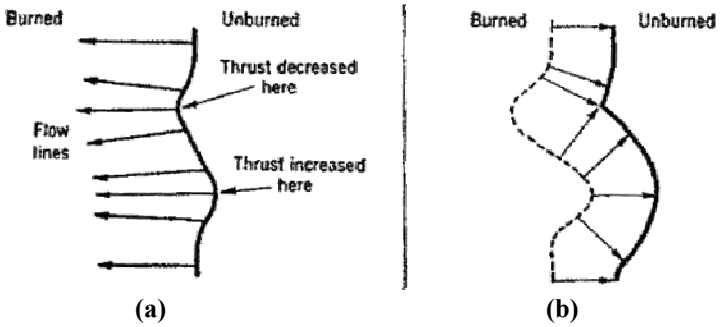

Figure 7 Hydrodynamic instabilities. (a) principle of hydrodynamic instability, (b) stabilizing effect of wave propagation (Manton et al., 1951).

In Figure 7a, it is shown that an indention with concave curvature toward the burned gas has converging lines of mass flow, therefore increasing the thrust at the indention causing it to grow with time. Similarly, an indention with convex curvature toward the burned gas side has diverging lines of mass flow, decreasing the thrust at the indention and causing it to also grow with time. However, due to the fact that the flame front moves as a wave, the largest size that these disturbances could attain is limited. This is shown graphically in Figure 7b. If the flame front were stationary, the disturbances shown in Figure 7a would take the shape and size of the dotted line in Figure 7b. However, because the flame front is moving

as a wave, the disturbances actually take the form of the solid line in Figure 7b. This reasoning shows that convex indentations will tend to vanish as the flame propagates, and that concave disturbances will tend to flatten out as the base becomes wider. If this theory were the only mechanism behind flame instabilities, then a steady state condition would be reached where the increase in cell curvature due to increased thrust would be balanced by the decrease in cell curvature due to the wave propagation (Manton et al., 1951).

Diffusive Instabilities

Diffusive instabilities were first studied by Manton et al. (1951). In studying flame front instabilities, they discovered that both slow- and fast-burning mixtures could propagate with large, smooth areas, as well as become cellular and unstable. It was noted that one of the characteristics of the mixtures that became unstable was that the deficient component was also the component of largest diffusivity. They therefore theorized that the primary cause of cellular break-up was the diffusional change of mixture composition in the curved regions of the flame, as shown by Figure 8.

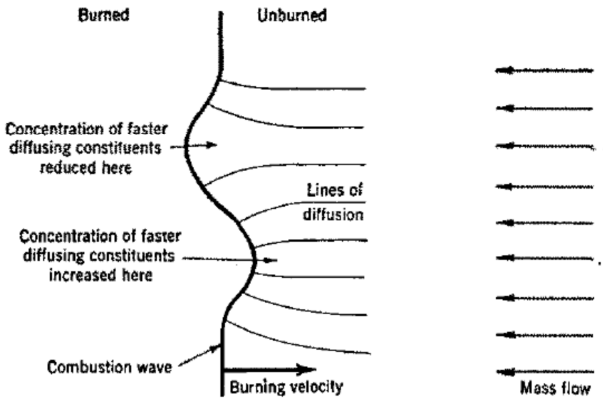

Figure 8 Illustration of the principle of diffusional change at the flame front (Manton et al., 1951).

Two different cases can occur in Figure 8, depending on the relative diffusivity of the fuel and oxidizer. When the mass diffusivity of the fuel into the diluent is greater than the mass diffusivity of the oxidizer into the diluent, the equivalence ratio is rendered leaner at the indentations convex toward the burned gas, while the mixture becomes richer near the indentations concave toward the burned gas. For the second case, the opposite effect is present. If the mass diffusivity of the fuel into the diluent is less than the mass

diffusivity of the oxidizer into the diluent, then the mixture becomes richer at the convex indentations while becoming leaner at the concave indentions.

This behavior promotes different results based on both the equivalence ratio and relative diffusivity of the fuel and oxidizer. For example, if a mixture has the diffusivity ratio as described in the first case, a lean mixture will be diffusively unstable while a rich mixture will exhibit enhanced stability. This result is because a lean mixture of this diffusivity ratio will have the local flame speed decreased at the convex indentations and increased at the concave indentions due to the variation of flame speed with equivalence ratio. This variation will result in the growth of both the convex and concave regions. However, a rich mixture of this diffusivity ratio will have the local flame speed increased at the convex regions and decreased at the concave regions. This rich-mixture trend will lead to the decay of both the disturbances. Figure 9 gives a graphical description of the change in local flame speed and the effect on stability for both cases.

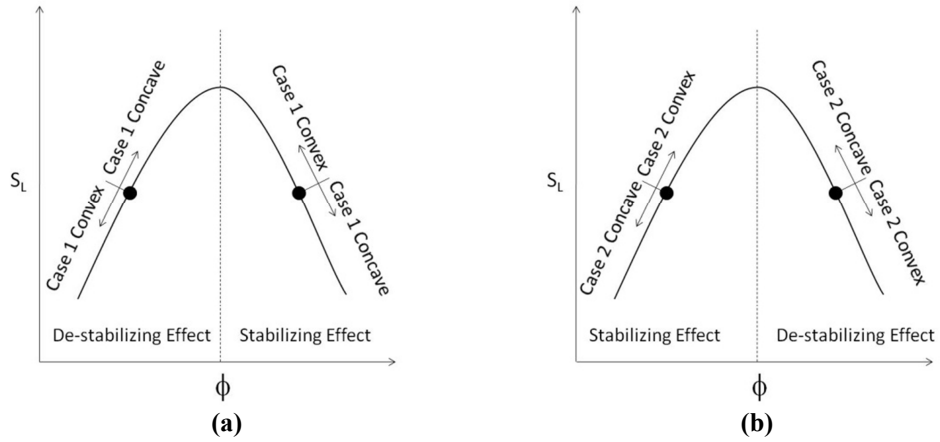

Figure 9 Graphical description of local flame speed variation with equivalence ratio. (a) Case 1, (b) Case 2.

More recently, a connection has been made between the Lewis number and the changes in stability for a mixture. The Le is a measure of the relative influence of thermal-to-mass diffusion for a mixture of gases (Law, 2006). This non-dimensional number plays a large role in the flame response for a given mixture

(Tsuji and Yamaoka, 1982; Law, 1988, 2008; Sun et al., 1999) and can actually give insight into the way that stretch may affect a flame. It has been experimentally shown that diffusion can have both a stabilizing and de-stabilizing effect on flames, and most often, mixtures with Le greater than 1 are considered diffusionally stable, whereas mixtures with a Le less than 1 are considered diffusionally unstable. One of the goals of this thesis was to correlate the theoretically predicted Le numbers with the critical radii of the measured flames.

CHAPTER III

EXPERIMENTAL SETUP

3.1 Facility Description

The flame speed facility used in this study consists of a constant-volume cylindrical vessel with optical access, a Z-type schlieren setup with high-speed camera, a vacuum system, a gas-handling manifold, and an ignition system. The facility also includes a blast wall and separate control room. After the short time period that the flame is measured, the pressure in the vessel increases by approximately a factor of 10. Though the apparatus has been designed to withstand this increase in pressure, the cylindrical vessel and optical setup are located behind a steel-reinforced, concrete-filled blast wall for safety reasons. To fill, vent, or vacuum the vessel, pneumatic valves are operated from outside the blast wall near the gas manifold. This remote operation allows for mixtures to be created and then filled into the vessel without entering the room containing the vessel. The door to the blast room is closed before making a mixture and remains closed until after the experiment is over. A final level of safety is provided by running the experiment from a separate control room. From this room, the camera settings and ignition energy across the electrodes can be adjusted before igniting the mixture. Figure 10 shows the floor plan layout of the facility.

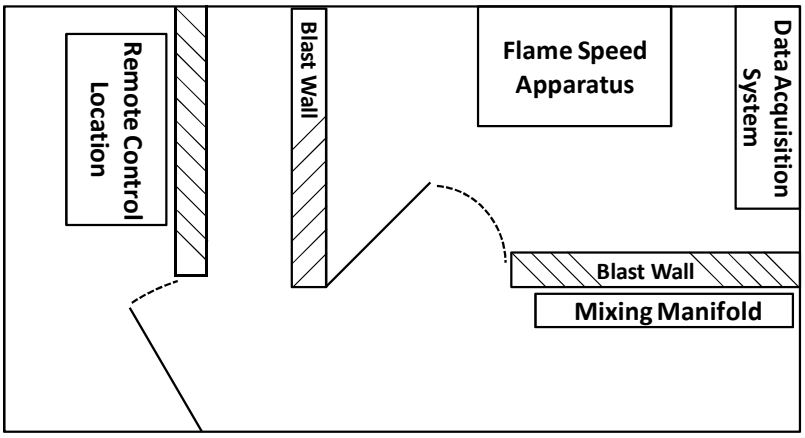

Figure 10 Floor plan layout of experimental facility.

3.2 Hardware

The constant-volume bomb used herein is a cylindrical vessel with an inside diameter of 30.5 cm, an outside diameter of 38.1 cm, and an internal length of 35.6 cm. Optical access is provided by two fused quartz windows 20 cm in diameter and 6.35-cm thick, clamped between neoprene gaskets with stainless steel spacers to shield the gaskets from the hot gases. This leaves 12.7-cm diameter clear apertures on each side. The vessel is constructed from 7075-T6 aluminum alloy and is capable of 15-atm initial pressures. The internal pressure of the vessel is continuously monitored via an Endevco 8511A piezo-resistive pressure transducer (0-689 bar). The signal from the transducer is then fed to a GageScope PCI (5 MHz, 16 bit resolution) data acquisition system. Figure 11 and Figure 12 show a schematic of the vessel and a picture of the vessel in operation, respectively.

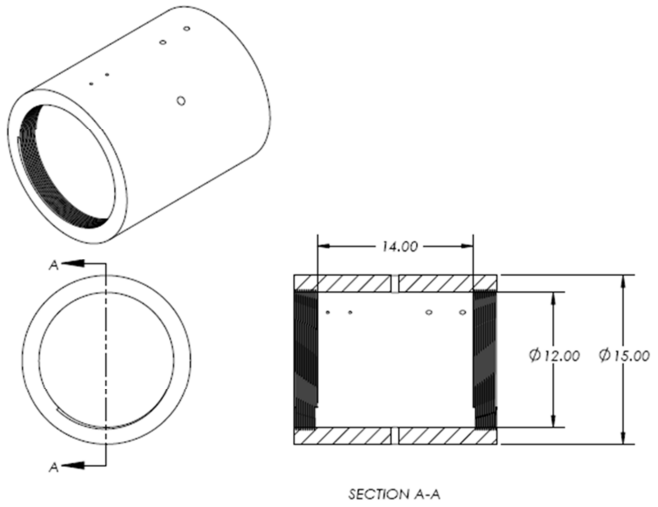

Figure 11 Drawing for flame speed vessel with dimensions shown in inches.

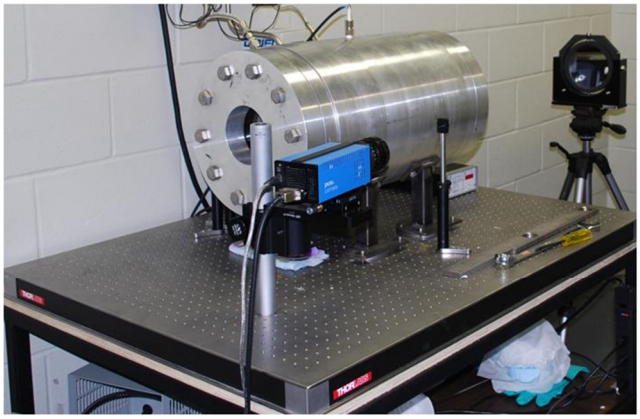

Figure 12 Picture of flame speed vessel and optical setup.

Mixtures are made using a manifold, shown schematically and in operation in Figure 13 and Figure 14, located outside of a concrete-filled, steel-reinforced blast wall room that contains the flame speed vessel. The partial-pressure method is used to make mixtures, and the pressures are monitored via 0-1000 Torr and 0-500 psi pressure transducers. In the multi-fuel mixtures, a separate mixing tank is used to mix the fuels before introducing them into the vessel. This gas combination is allowed to mix for a period of 2 days to verify that the two fuels are completely mixed. The purity of the gases used in this study is summarized in Table 1.

Table 1 Gas purity summary

Gas	Grade	Purity
CH_4	3.7	99.97%
C_2H_6	3.5	99.95%
C_3H_8	Instrument	99.5%
CH_3OCH_3	2.6	99.6%
O_2	UHP	99.999%
N_2	UHP	99.999%

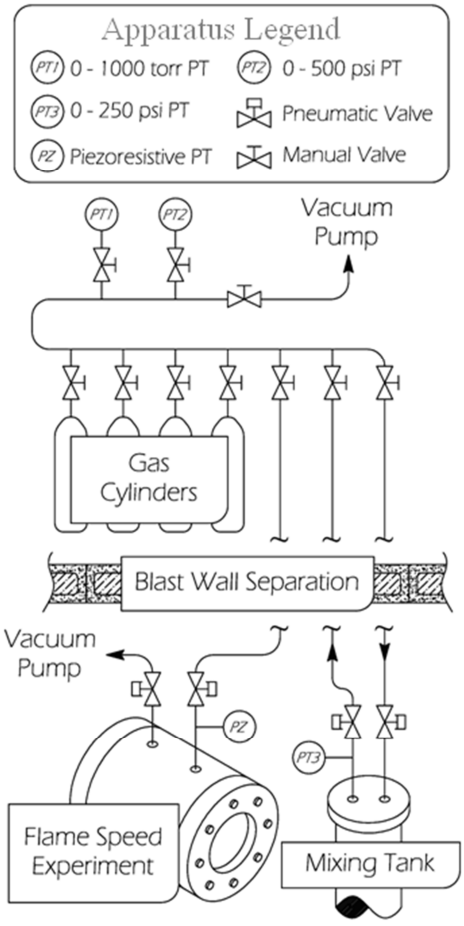

Figure 13 Schematic of mixing manifold for flame speed apparatus.

Figure 14 Picture of mixing manifold for flame speed apparatus.

The ignition system consists of an adjustable, constant-current power supply (GwInstek GPR-1810HD), a 10-μF capacitor, an automotive coil, and a solenoid switch. The ignition energy is minimized before each experiment by adjusting the power supply to the minimum amount needed to create a spark across the electrodes. The electrodes are 0.9-mm (0.035-in) diameter Alloy X rods, sharpened at the tips and set at a variable gap. A variable gap is needed because the ignition energy varies with mixture composition and initial pressure, and care is taken to ensure that the minimum ignition energy is always used in each experiment to avoid the spark energy from influencing the speed of the flame.

3.3 Optical Technique

The experimental data are taken using a Z-type schlieren system as described by Settles (2006). Figure 15 shows a schematic of the optical setup. A mercury arc lamp provides the light source for the schlieren system. Light is passed through an f/8 condenser lens and a circular aperture before being reflected through the vessel via a 15.2-cm, f/8 parabolic mirror. After the test section, the parallel light is reflected off another 15.2-cm, f/8 parabolic mirror. Then the light is passed through a circular pinhole aperture, adjustable from 1 to 11 mm diameter, at the focal point of the second mirror where it cuts off the steered light caused by the density gradients. A circular pinhole aperture was found to resolve the image better than a vertical knife edge (Bourque et al., 2008). The image is then projected into a high-speed camera and recorded. Example images from this study are provided in Figure 16 to show the quality of images taken herein and to highlight the differences between 1-, 5-, and 10-atm initial pressure experiments. The time step in Figure 16 is normalized to the first image presented.

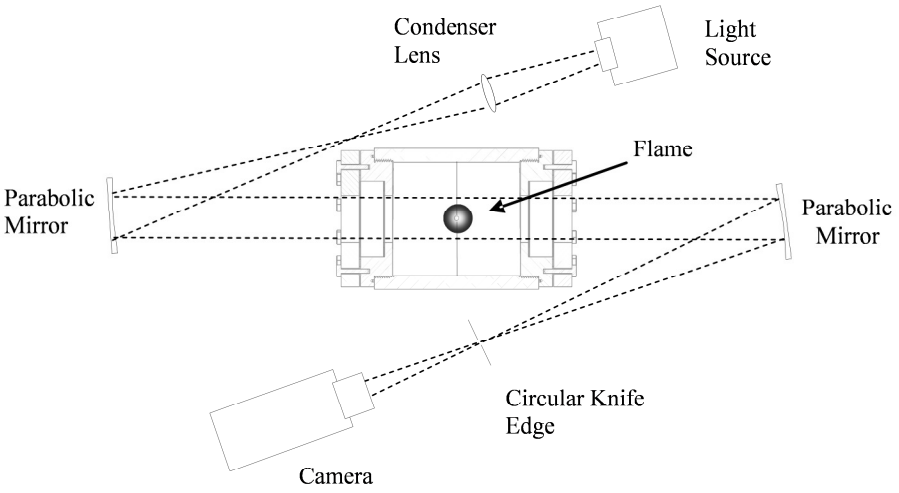

Figure 15 Optical setup for high-speed schlieren system.

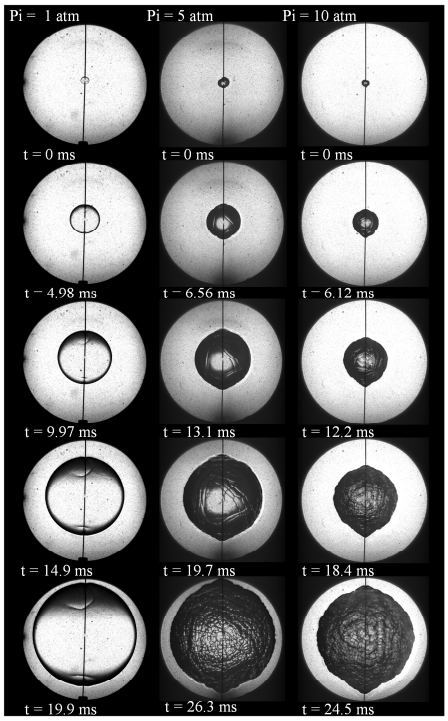

Figure 16 Flame images for 1 (left), 5 (middle), and 10-atm (right) stoichiometric 60/40 CH_4/C_2H_6 at initial pressures of 1, 5, and 10 atm.

3.4 Constant-Pressure Assumption

When measuring the laminar flame speed of a fuel-oxidizer mixture using a constant-volume vessel, it is important to ensure that the pressure remains constant for the duration of the measurement to avoid non-ideal pressure effects and flow disturbances. Due to the large internal size of the vessel used in this study, the pressure remained constant during the measurement of the flame propagation. This is verified by Figure 17, where a normalized pressure trace is shown versus time, with flame images marking the relative times that the flame measurements were taken. Additionally, flame radii up to 4.6 cm can be measured without significant deviations from constant-pressure behavior (Burke et al., 2009).

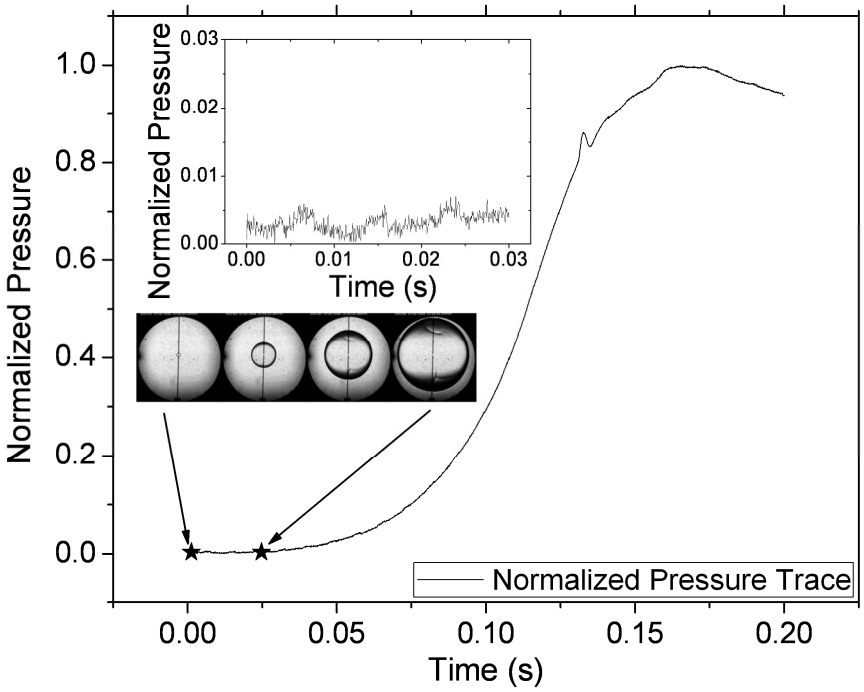

Figure 17 Experimental pressure trace showing time period of measurement. The inset figure shows a closer view of the constant-pressure measurement time period.

CHAPTER IV

ANALYSIS AND UNCERTAINTY

4.1 Data Analysis

In this study, radii from 0.7 to 4.5 cm were used to determine the laminar flame speed and Markstein length. These radii correspond to less than 30% of the inner radius of the vessel. Therefore, the effect of confinement can be neglected for flame radii used in this study with less than 3% error (Burke et al., 2009). Flame images were converted into flame radii by using the methodology outlined in Figure 18. More detailed information on this technique is available in de Vries (2009). For each flame image, six points are selected 45° apart from each other and 45° from the electrodes on the outer radius.

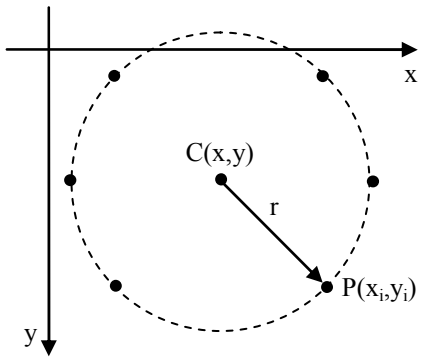

Figure 18 Flame radii determination methodology.

A best-fit algorithm using a least-squares estimator based on the Euclidean distance between the point and the circle, given by Eq. (22), was used.

$$J = \sum_{i=1}^{n} (d_i - r)^2 \quad \textbf{(22)}$$

Here, $d_i = \sqrt{(x_i - x)^2 + (y_i - y)^2}$, the Euclidean distance between the point P(x_i, y_i) and the center of the circle C(x,y). The algorithm used in this study uses the Levenberg-Marquardt algorithm to minimize *J* (Shakarji, 1998). This fitting methodology allows for the center of the circle to be tracked instead of being

defined. Therefore, buoyancy effects can be measured and do not affect the experimental results. These small buoyant forces can be seen in Figure 19 as a rise in the center of the circle as a function of time.

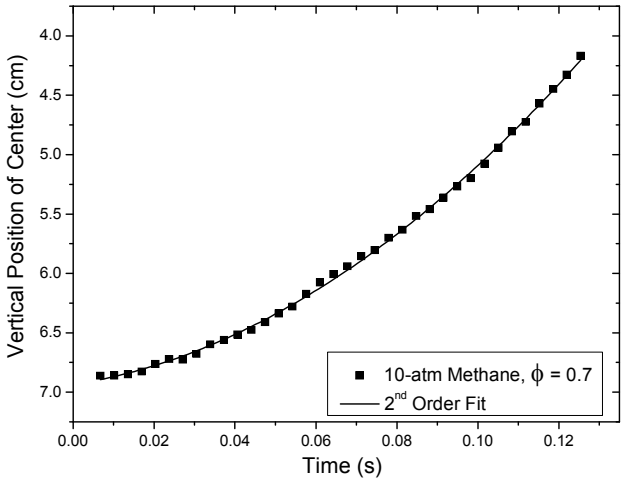

Figure 19 Buoyancy effect shown by the rise of flame center for pure methane at an equivalence ratio of 0.7 and 10-atm intial pressure.

The instantaneous flame radius given by the image post-processing is analyzed using the linear relationship given by Eqs. (23-26) (Markstein, 1964; Dowdy et al., 1990; Brown et al., 1996).

$$S_b = S_b^o - L_{m,b}\alpha \tag{23}$$

Where S_b is the burned, stretched flame speed, S_b^o is the burned, un-stretched flame speed, $L_{m,b}$ is the burned Markstein Length, and α is the flame stretch defined by

$$\alpha = \frac{1}{A}\frac{dA}{dt} = \frac{1}{4\pi R^2}\frac{d(4\pi R^2)}{dt} = \frac{2}{R}\frac{dR}{dt} \tag{24}$$

After substituting Eq. (24) into 23, the result can be integrated to give Eq. (25), where R_f is the instantaneous flame radius and *t* is the corresponding time.

$$R_f = S_b^o t - 2L_{m,b}\ln(R_f) + const \tag{25}$$

The un-stretched flame speed S_b^o and Markstein length $L_{m,b}$ are then obtained by using linear regression. The un-burned, un-stretched flame speed $S_{L,u}^o$ and Markstein length $L_{m,b}$ are found by dividing the burned values, S_b^o and $L_{m,b}$ extracted from Eq. (25), by the density ratio across the flame given by Eq. (26).

$$\sigma = \frac{\rho_u}{\rho_b} \tag{26}$$

It is important to provide the calculated density ratio when presenting data, as this ratio plays a large role in the final analysis of the data. The density ratio was calculated using the Equilibrium module in Chemkin (CHEMKIN-PRO 2008) with the authors' chemical kinetics model as the input. It was observed that using different kinetics models resulted in different density ratios. This result is due to the fact that some models include molecules that others do not. The inclusion of NO_x chemistry in some models resulted in density ratios that were as much as 0.02 smaller than the ratios used herein. Though this seems like a small discrepancy, the different density ratios can result in up to 0.25-cm/s difference in the un-stretched, unburned laminar flame speed.

4.2 Residual Analysis

Flame acceleration due to cellularity and instabilities was taken into account by performing a residual analysis. Residuals, the difference between experimental radii and the predicted radii, are plotted versus flame radius to determine where the flame becomes unstable. The predicted radii are solved for using an iterative method. First, the flame speed, Markstein length, and offset are found using linear regression on the experimental data. Then, the experimentally determined flame speed, Markstein length, and offset are input to Eq. (25), the integrated Markstein relation. In Eq. (25), all the values are now known except for the time and radius at each time step. Finally, the predicted radius is found by iteratively adjusting the radius until the resulting time matches each experimental time step to within 0.000001 second. The predicted radius is now compared to the experimentally measured radius, shown by Figure 20. Since the residuals are initially centered about zero, the flame can be assumed to propagate linearly. Additionally, flame acceleration is easily seen using this method. When the residuals are no longer centered about zero, the flame is considered unstable. This method provides a quantitative way to determine where the flame becomes unstable. In contrast, determining flame acceleration via visual analysis of the recorded images is a subjective process that may give different results depending on the person performing the analysis.

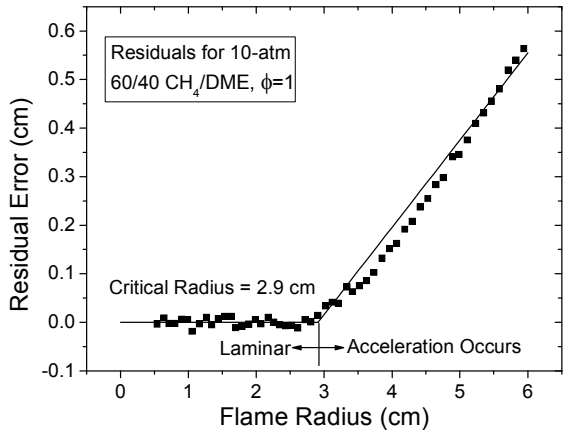

Figure 20 An example of a residuals plot showing flame acceleration.

4.3 Lewis Number Calculations

The Lewis number, Le, is a ratio of thermal diffusion to mass diffusion, given by Eq. (27). This dimensionless number plays a large role in the flame response for a given mixture (Law, 1988; Sun et al., 1999; Tsuji and Yamaoka, 1982).

$$L_e = \frac{\lambda}{C_p \rho D_{i,j}} \tag{27}$$

In Eq. (27), λ is thermal conductivity, ρ is density, C_p is specific heat, and $D_{i,j}$ is the mass diffusivity between i and j. To calculate the mixture Lewis numbers, the above properties were found for each mixture. The mixture-averaged thermal conductivity was calculated using Eq. (28), where X_k is the mole fraction of k and λ_k is the thermal conductivity of species k (Kee et al., 1986).

$$\lambda_{mix} = \frac{1}{2}\left(\left(\sum_{k=1}^{K} X_k \lambda_k\right) + \frac{1}{\sum_{k=1}^{K} \frac{X_k}{\lambda_k}}\right) \tag{28}$$

The mixture specific heat was calculated as shown by Eq. (29).

$$C_p = \sum_{k=1}^{K} C_{p,k} Y_k \tag{29}$$

In Eq. (29), $C_{p,k}$ is the specific heat of species k, and Y_k is the mass fraction of species k. The mixture densities were taken directly from the output file used to solve for the density ratio in the data analysis

(Reynolds, 1986). The mass diffusion coefficient between species i and j was based on the deficient species diffusing into the diluent (Tsuji and Yamaoka, 1982). To calculate the mixture mass diffusivity of the fuel blends, the properties of the fuels were mass averaged to find the needed parameters such as σ and ε/k_b. The diffusion calculations for the fuel blends were then done following the aforementioned method. The previous method of averaging the needed diffusion parameters was done to calculate and suggest a method for calculating Le for multi-fuel-blend mixtures that have not been previously published in literature. The Le was resolved by calculating the diffusion coefficient as the deficient species diffusing into the diluent and using Eqs. (27-28) are accurate for sufficiently off-stoichiometric mixtures (Sun et al., 1999). However, the Lewis number calculations presented herein are not intended to give the most accurate results, but are used to show general trends between fuels and their blends.

4.4 Uncertainty Analysis

This section includes an overview of the uncertainty analysis performed. In the analysis presented, both systematic and random uncertainties were taken into account using the methods outlined by Moffat (1988). The total experimental uncertainty is given by Eq. (30), where B_{SL} is the systematic uncertainty and P_{SL} is the random uncertainty at a 95% confidence interval.

$$U_{S_L} = \sqrt{B_{S_L}^2 + P_{S_L}^2} \tag{30}$$

The systematic uncertainty, given by Eq. (31), includes u_i, the fixed error for each variable x_i, and S_L the relationship between the flame speed and each variable x_i.

$$B_{S_L} = \sqrt{\sum_{i=1}^{n} \left(\frac{\partial S_L(x_i)}{\partial x_i} u_i \right)^2} \tag{31}$$

To use this definition of the systematic uncertainty, a relationship between each independent variable and the flame speed had to be known. Using the experimental results of this study, a relationship of the following form is proposed, where P_i is the initial pressure in atmospheres, and ϕ is the equivalence ratio.

$$S_{L,u}^{o} = \left(a + b*\phi + c*\phi^2\right) * \left(1/P_i \right)^{\left(d + e*\phi + f*\phi^2\right)} \tag{32}$$

Table 2 provides the coefficients for the correlation shown by Eq. (32) for the fuels in this study. In addition, Figure 21 shows the correlation against experimental ethane data. The present data compared to the correlation are shown here for convenience and are properly discussed in the Results section.

Table 2 Correlation coefficients for Eq. (32) for the mixtures in this study

	CH_4	C_2H_6	60/40 CH_4/C_2H_6	80/20 CH_4/C_2H_6	C_3H_8	80/20 CH_4/C_3H_8	DME	60/40 CH_4/DME	80/20 CH_4/DME
a	-141.4	-98.3	-118.7	-122.7	-99.0	-116.0	-110.6	-129.0	-129.5
b	331.5	250.2	289.2	294.9	243.5	274.5	270.3	309.7	308.0
c	-156.2	-114.2	-134.7	-137.4	-107.8	-123.8	-117.5	-141.5	-142.5
d	2.59	1.16	2.47	2.46	1.35	2.73	1.38	2.09	2.31
e	-4.39	-1.80	-4.35	-4.31	-2.06	-4.78	-2.12	-3.38	-3.88
f	2.17	0.84	2.11	2.13	0.96	2.32	0.98	1.61	1.90

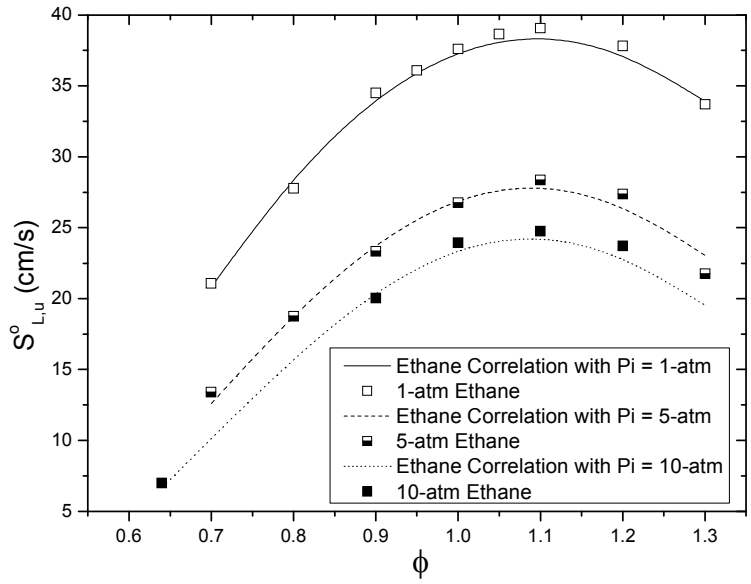

Figure 21 Experimentally obtained ethane correlation compared to ethane data from the present study.

The uncertainty of each variable in the flame speed correlation (Eq. [32]) was performed by assuming the worst case of error for the pressure. Since the mixtures were made using a partial pressure method, the error in pressure not only directly influences the flame speed as shown by the correlation, but also indirectly through equivalence ratio errors. The flame speed is a much stronger function of equivalence

ratio than pressure, but the error in pressure drives the error in both the equivalence ratio and more importantly the flame speed. The uncertainty of each transducer used is 0.25% of the reading for both the MKS 0-1000 Torr transducer and the 0-250 psi Setra transducer. The 0-1000 Torr transducer is used when possible due to the higher accuracy of the readout. The 0-250 psi readout box shows only to the nearest 0.1 psi, while the 0-1000 Torr gauge reads to ~ 0.002 psi. Table A13 in the Appendix shows characteristic uncertainties for the equivalence ratio and initial pressure, assuming that the transducer read on the low side when filling the vessel with fuel and assuming that the transducer read on the high side when filling the vessel with oxygen, resulting in the largest error in equivalence ratio possible.

From Figure 21, it is clear that the correlation fits the experimental data very well, and similar agreement is seen for the other fuels studied. The random uncertainties in this study are described by Eq. (33). Here y_i is the experimental value, y_{ci} is the predicted value from the mth order polynomial (Eq. [32]), N is the total number of data points, and ν is the degrees of freedom, N – (m + 1).

$$S_{yx} = \left(\frac{\sum_{i=1}^{N} \left(y_i - y_{ci} \right)^2}{\nu} \right)^{1/2} \tag{33}$$

The precision interval at a 95% confidence level becomes $P_{S_L} = \pm t_{\nu,0.95} S_{yx}$. The total uncertainty in this study covered a large range, from as little as 0.3 cm/s to 3.5 cm/s considering all of the cases investigated. This result is an acceptable range of uncertainty for the measurements, though when viewed as a percentage they seem large. The largest percentage uncertainty was near 40%, and this value is due mainly to two factors. First, for this large uncertainty, the value of the measured flame speed was quite small, near 7 cm/s. Therefore, an uncertainty value of a few cm/s results in a large percentage uncertainty. Second, the laminar flame speed is sensitive to the initial temperature, so fluctuations in room temperature can have an effect on the measured flame speed. According to modeling results, a few Kelvin change in initial temperature can change the measured flame speed by up to 0.5 cm/s. In our uncertainty analysis, the effect of temperature was neglected because the sensitivity to initial temperature for each fuel was not

previously described in the literature, and it could not be measured using the experimental apparatus described herein. Therefore, though the percentage uncertainty seems high for a few cases, the actual value of the uncertainty is reasonable for these types of measurements. Tables A10 –A11 in the Appendix show the full results for the uncertainty analysis of all the conditions investigated herein, including both the actual value of the uncertainty and on a percentage basis. A characteristic uncertainty for the data is shown on Figure 23 and Figure 24.

4.5 Chemical Kinetics Modeling

Simulations were performed using the Premix module in the CHEMKIN-PRO (2008) package with the C4 (Petersen et al., 2007), JetSurF (Egolfopoulos et al., 2009), San Diego (San Diego, 2005), and GRI 3.0 (Smith et al., 1999) mechanisms as inputs. For the C4 mechanism, adjustments were performed through collaboration with the National University of Ireland Galway, Combustion Chemistry Centre. The experimental data presented herein were used as tuning targets for the kinetics model, as well as previous ignition delay time measurements performed at Texas A&M. The detailed chemical kinetics mechanism is based on the hierarchical nature of hydrocarbon combustion mechanisms containing the H_2/O_2 sub-mechanism (O'Conaire et al., 2004), together with the CO/CH_4 and the C2 and C3 sub-mechanisms that have already been published (Petersen et al., 2007; Healy et al., 2008a, 2008b). The C4 sub-mechanism has been fully detailed in two recent papers on the butane isomers (Healy et al., 2010a, 2010b).

Several updates were made to the mechanism to improve agreement to the current dataset with the most pertinent discussed below (all changes are included as comments in the CHEMKIN input file). The most significant change to the mechanism was the adoption of ethyl and vinyl radical decompositions from Miller and Klippenstein (2004), causing a marked improvement in the prediction of the high-pressure ethane flame speeds. The low-pressure limit rate expression for ethyl reaction was reduced by 66 percent to improve overall agreement. To improve model predictions of the high-pressure methane data, the rate of methane decomposition to methyl radical and H atom was taken from GRIMECH 2.11 (Bowman et al., 1995) and the high- and low-pressure limits reduced by fifty and thirty percent, respectively.

The DME sub-mechanism is based on Fischer et al. (2000) and Curran et al. (2000) with minor updates on the low-temperature chemistry that have no effect on flame speed predictions; this part of the work is ongoing and is not detailed. One of the most sensitive reactions as far as laminar flame speed is concerned is $H + CH_3 + M = CH_4 + M$ for both CH_4/air and DME/air systems and their binary mixtures; this reaction is pressure dependant and therefore becomes more sensitive at higher pressures. To get better agreement at high pressures, the rate constant of this reaction was revised during the present study; specifically, the rate constant expression in the GRI 2.11 mechanism (Bowman et al., 1995) has been taken as the basis, and both high- and low-pressure limit A factors were decreased within uncertainty limits. A sensitivity analysis for a stoichiometric 60/40 CH_4/DME mixture is presented in Figure 22. The initial version of the model used in the current work is C4-49, which is available online together with associated thermochemical parameters at http://c3.nuigalway.ie/mechanisms.html. To save computation time, all the simulations were performed with a C3 version of this mechanism with low-temperature reactions and species removed.

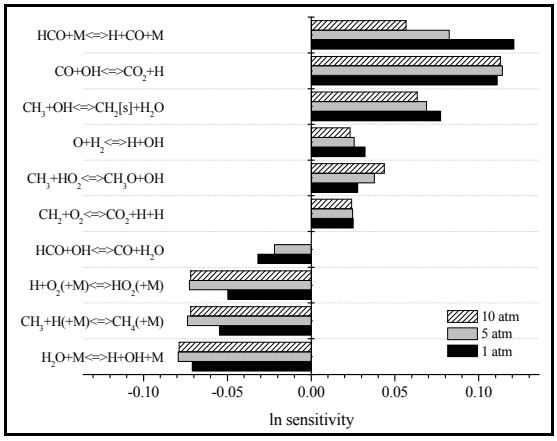

Figure 22 Flame speed sensitivity analysis for a 60/40 CH_4/DME mixture with an equivalence ratio of φ = 1.0 at pressures of 1, 5 and 10 atm. The sensitivity of the reaction $H + O_2 = OH + O$ is the dominant one but is not shown to accentuate the sensitivities of the other reactions.

A sensitivity analysis was performed for a 60/40 CH_4/DME mixture at $\varphi = 1.0$, shown in Figure 22. In general, the system is most sensitive to the high-temperature chain branching reaction $H + O_2 \rightleftarrows O + OH$; however this reaction is omitted on the plot in Figure 22 for sake of clarity. Reactions with positive sensitivity coefficients are promoting reactivity, while ones with negative coefficients are inhibiting. Recombination of CH_3 and H into methane is an inhibiting reaction competing with the chain branching for H atoms, which the system is very sensitive to at all pressures. Adjusting the rate constant of this reaction improved our results significantly, especially at 5 and 10 atm conditions, as mentioned above.

CHAPTER V

RESULTS AND DISCUSSION

The range of experimental conditions investigated covers measurements of the pure fuels CH_4, C_2H_6, C_3H_8, and CH_3OCH_3. Also investigated herein are 60/40 blends of CH_4/C_2H_6, CH_4/CH_3OCH_3 and 80/20 blends of CH_4/C_2H_6, CH_4/C_3H_8, and CH_4/CH_3OCH_3. The results for pure CH_4, C_2H_6, and C_3H_8, as well as an 80/20 blend of CH_4/C_2H_6 have been previously presented by de Vries (2009), but have been shown here for comparison purposes. The following sections present and compare the results for the pure fuels, blends, and the trends in Lewis number and critical flame radii. Additionally, modeled results are compared to the experimental measurements and discussed.

5.1 Pure Fuel's Flame Parameters

The results for the pure CH_4, C_2H_6, C_3H_8, and CH_3OCH_3 are fully treated elsewhere (de Vries et al., 2009; de Vries et al., 2010), but are included here for ease of comparison. In Figure 23, the flame speed results for pure CH_4 at initial pressures of 1, 5, and 10 atm are compared to four chemical kinetics models. The four models used for comparison in this study are GRI (Smith et al., 1999), JetSurF (Egolfopoulos et al., 2009), San Diego (San Diego, 2005), and Curran's C4 mechanism (Petersen et al., 2007).

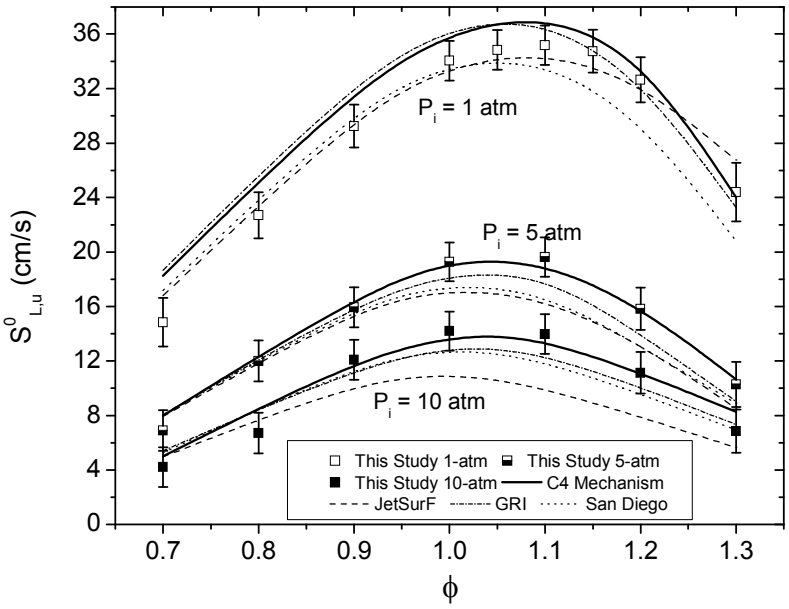

Figure 23 Pure CH_4 flame speed results for initial pressures of 1, 5, and 10 atm.

Figure 23 shows good agreement between the experimental data shown and the C4 kinetics model. Some discrepancies are seen between the predicted results amongst the models, with the JetSurF mechanism under predicting the experimental results by the largest amount as the pressure is increased. The pure CH_4 results have been previously validated against other experimental studies (de Vries, 2009), so comparisons with other researchers have been omitted in this study for figure clarity. Also in Figure 23 are uncertainty bars showing the results of the uncertainty analysis performed. It is seen that the uncertainty decreases as the plot nears the peak flame speed, and this trend is expected since the flame speed is less sensitive to equivalence ratio in this area. In Figure 24, the measured laminar flame speed of pure C_2H_6 is compared to the predicted results of the previously discussed kinetics models.

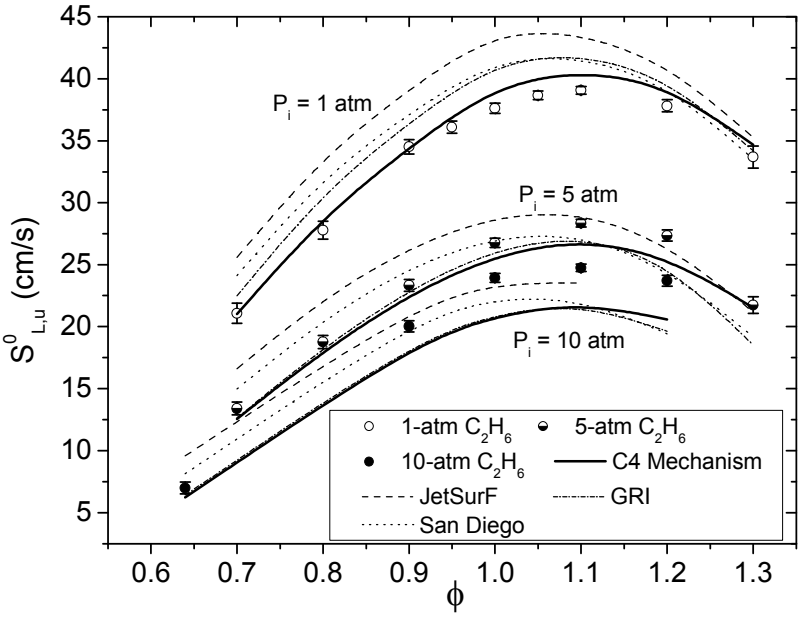

Figure 24 Pure C_2H_6 flame speed results for initial pressures of 1, 5, and 10 atm.

For pure C_2H_6, the C4 kinetics model accurately predicts the atmospheric flame speed. However, as pressure increases, the C4 model tends to under predict the burning velocity. Additionally, the other three models over predict the atmospheric flame speed results, but as pressure increases to 10 atm, the models begin to under predict the flame speed. Once again, the experimental results shown for pure C_2H_6 have been validated against other experimental studies in de Vries (2009), so the comparisons are not shown here in. Finally, note the difference in the error bars between Figure 23 and Figure 24. These two figures are a good representation of the uncertainty seen in this study, from the high to low side, respectively. Also note that Figure 24 has a larger scale on the vertical axis, effectively shrinking the size of the error bars, so there is less difference between the two cases than first appears. The results for pure C_3H_8 at initial pressures of 1 and 5 atm are shown in Figure 25.

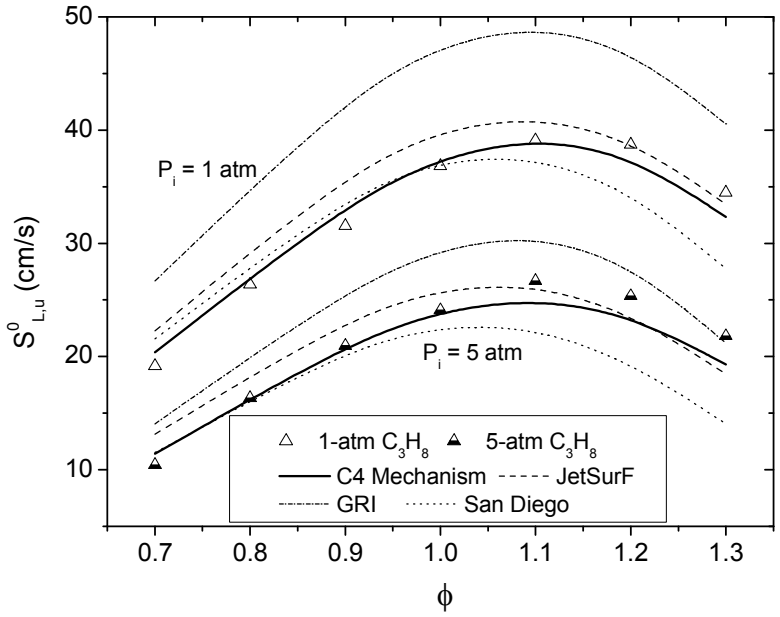

Figure 25 Pure C_3H_8 propane results for initial pressures of 1, 5, and 10.

As seen in Figure 25, the agreement between the experimental results presented and the C4 kinetics model for pure C_3H_8 is excellent for both initial pressures studied and for all equivalence ratios investigated. There is more scatter for the pure C_3H_8 model predictions than for the model predictions of the other pure fuels. The results for pure CH_3OCH_3 are shown in Figure 26.

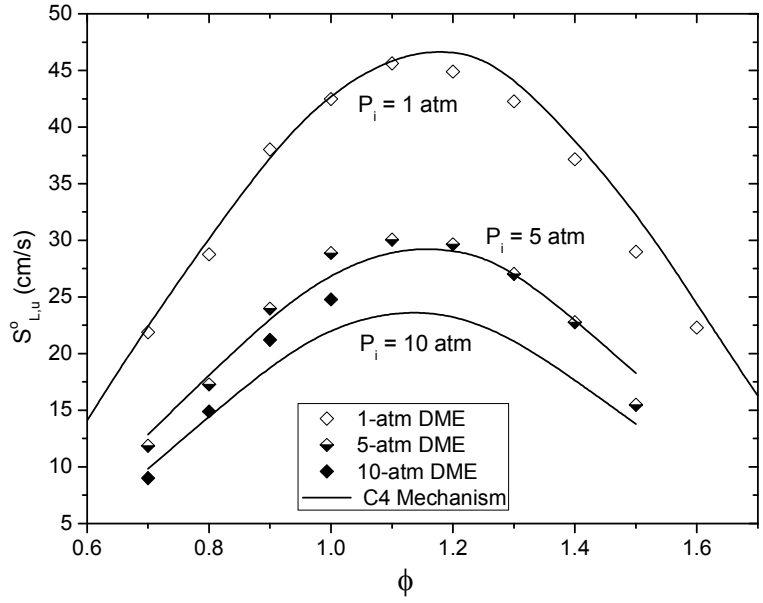

Figure 26 Pure CH_3OCH_3 results for initial pressures of 1, 5, and 10 atm.

As shown by Figure 26, agreement between the experimental data and the C4 mechanism is good for all the initial pressures and equivalence ratios studied. There is slight divergence for the 10-atm case, but the magnitude of the difference between the predicted and measured values is approximately 2.5 cm/s, only slightly larger than the uncertainty in the measurement. Also, only the C4 mechanism was compared to data in Figure 26, due to the fact that the JetSurF, GRI, and San Diego mechanisms do not contain CH_3OCH_3 chemistry.

5.2 Blended Fuel's Flame Parameters

After testing and verifying the pure fuel's burning properties, the flame response to blending was studied. It was of interest to not only measure the flame properties of the blends, but also to see if the C4 model was able to accurately predict the fuels' response to varying amounts of fuel mixtures due to its excellent agreement with the pure fuel values. Figure 27 gives the modeled and measured results for the 80/20 CH_4/C_2H_6 blend at initial pressures of 1, 5, and 10 atm.

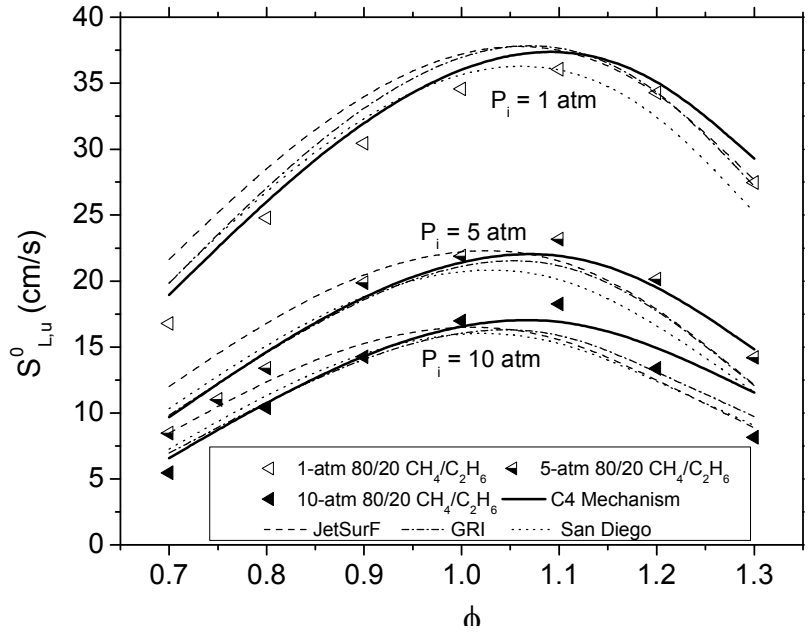

Figure 27 Flame speed results for 80/20 CH_4/C_2H_6 at initial pressures of 1, 5, and 10 atm compared to modeled results.

For the 80/20 CH_4/C_2H_6 blend, the C4 model shows the best agreement over the entire range of pressures and equivalence ratios studied. The other models do a decent job of predicting the flame speed, but the three other models tend to under predict the flame speed on the fuel rich side as pressure increases. The results of all the models tend to be an average of their predictions for the pure methane and pure ethane. Most notably, the San Diego mechanism under predicted the atmospheric pure methane results and over predicted the atmospheric pure ethane results, but here shows good agreement with the atmospheric 80/20 CH_4/C_2H_6 results. Figure 28 shows the measured and modeled results for the 60/40 CH_4/C_2H_6.

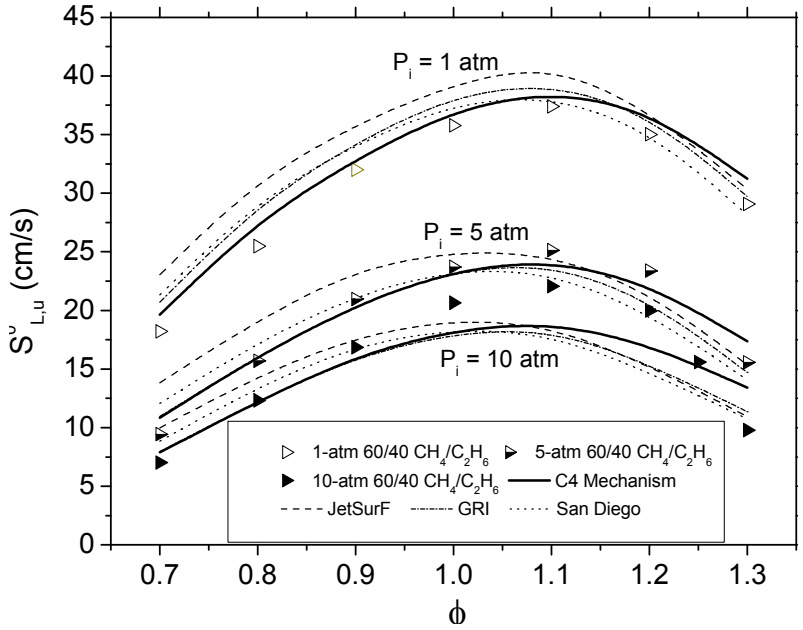

Figure 28 Flame speed results for 60/40 CH_4/C_2H_6 at initial pressures of 1, 5, and 10 atm compared to modeled results.

As the amount of ethane is increased to 40% by volume, the modeled response becomes more like the results for pure ethane. For example, the 10-atm initial pressure experimental results are under predicted by all the models and the amount of under prediction is affected by the ethane concentration. It is seen from Figure 27 and Figure 28 that the amount of under prediction at elevated pressures increases with ethane concentration. Though there is some slight divergence between the experimental and modeled results, in general, the model performs well, usually within the uncertainty of the flame speed measurement. Figure 29 gives the results for the 80/20 CH_4/C_3H_8 blend at 1 and 5 atm.

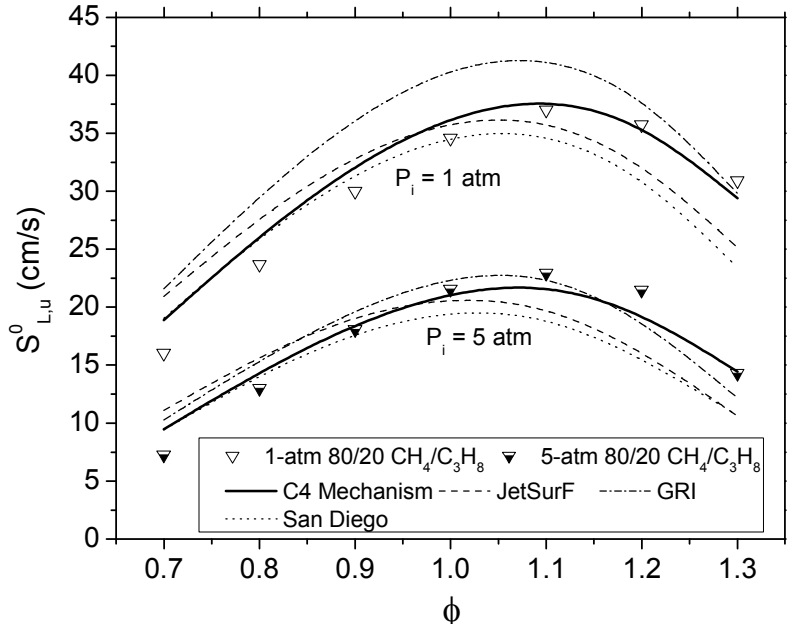

Figure 29 Flame speed results for 80/20 CH_4/C_3H_8 at initial pressures of 1 and 5 atm compared to modeled results.

For the 80/20 CH_4/C_3H_8 blend, the model accurately predicts the laminar flame speed, as expected due to the good agreement with both the pure CH_4 and C_3H_8. In comparison to the other models, the C4 mechanism does a better job representing the experimental data. Additionally, much like the pure C_3H_8 results, there is appreciable scatter between the other three models, with GRI over predicting the atmospheric flame speed and the San Diego mechanism under predicting the 1-atm data. Figure 30 and Figure 31 show the results of the 80/20 and 60/40 CH_4/CH_3OCH_3 experiments and modeling.

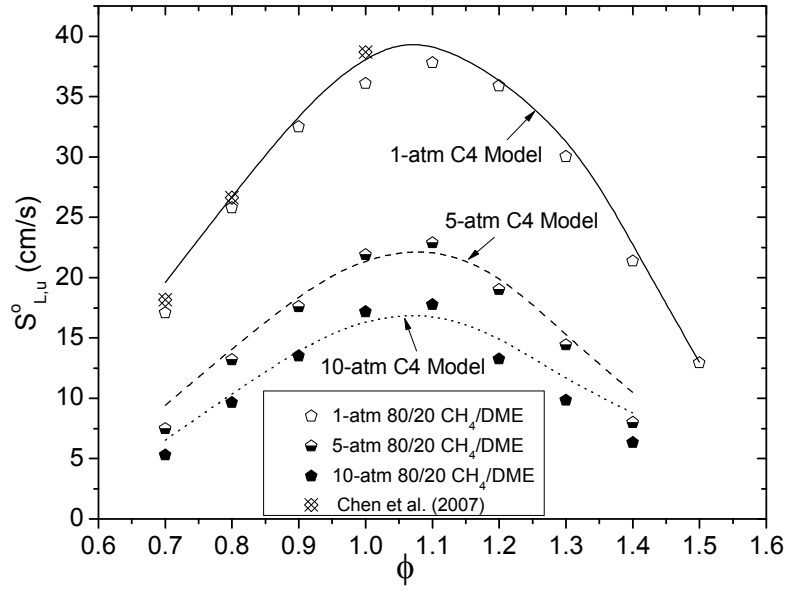

Figure 30 Flame speed results for 80/20 CH_4/CH_3OCH_3 at initial pressures of 1, 5, and 10 atm compared to modeled results.

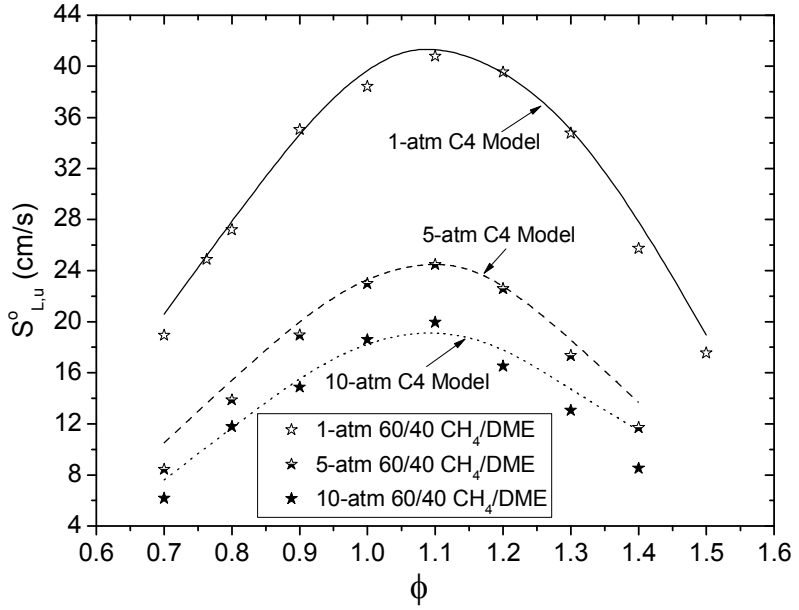

Figure 31 Flame speed results for 60/40 CH_4/CH_3OCH_3 at initial pressures of 1, 5, and 10 atm compared to modeled results.

In Figure 30 and Figure 31, the C4 model demonstrates good agreement with both CH_4/CH_3OCH_3 blends at all initial pressures investigated. The C4 model was the only model compared to experimental data because the JetSurF, GRI, and San Diego mechanisms do not define CH_3OCH_3 as a molecule. Additionally, a comparison between the data presented and previously published data by Chen et al. (2007) in Figure 30 shows close agreement between the two measurements.

5.3 Comparison of Pure Fuels and Blended Fuels

In this section, the flame speed of the pure fuels composing the blends is compared to the flame speed of the fuel blends. In the following section, the lines do not represent model predictions, but are shown to guide the eye through the data sets. Figure 32 compares the CH_4/C_2H_6 fuel blends.

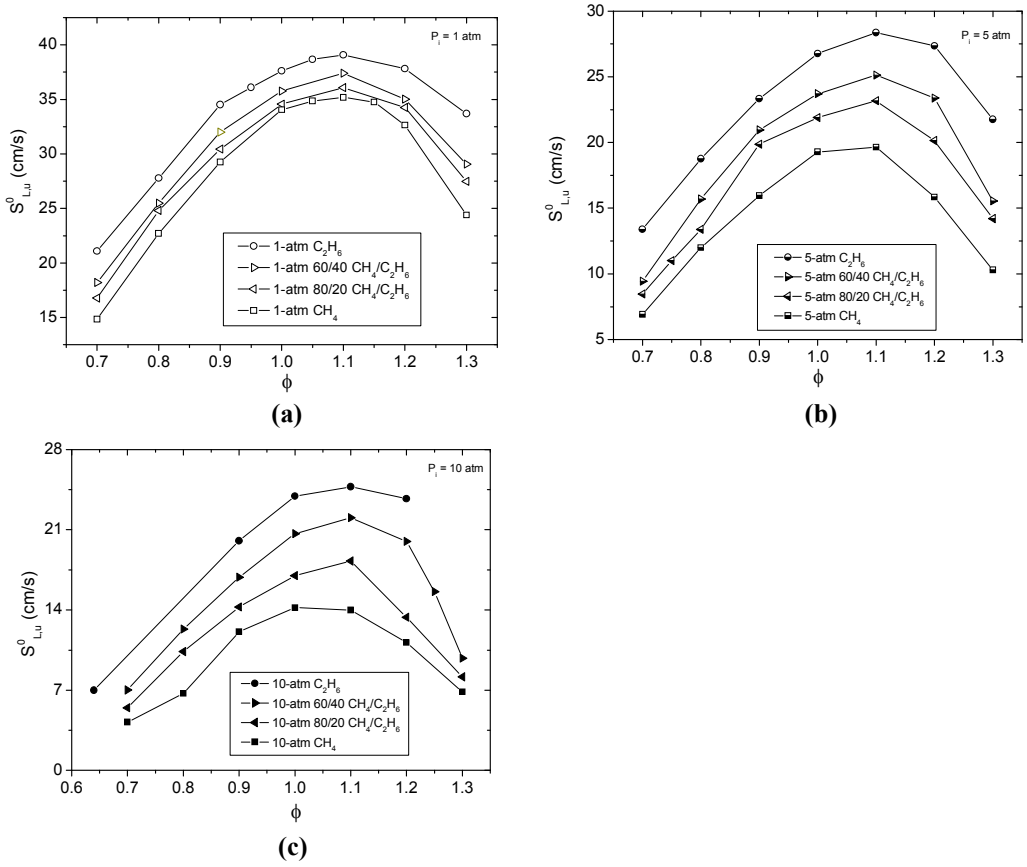

Figure 32 Results for CH_4/C_2H_6 laminar flame speeds. (a) Flame speed for 1-atm C_2H_6, 60/40 CH_4/C_2H_6, 80/20 CH_4/C_2H_6, and CH_4, (b) Flame speed for 5-atm C_2H_6, 60/40 CH_4/C_2H_6, 80/20 CH_4/C_2H_6, and CH_4, (c) Flame speed for 10-atm C_2H_6, 60/40 CH_4/C_2H_6, 80/20 CH_4/C_2H_6, and CH_4.

As expected, Figure 32 demonstrates that the flame speeds of the blends fall between the pure fuels' flame speeds. This trend is seen for all initial pressures studied.

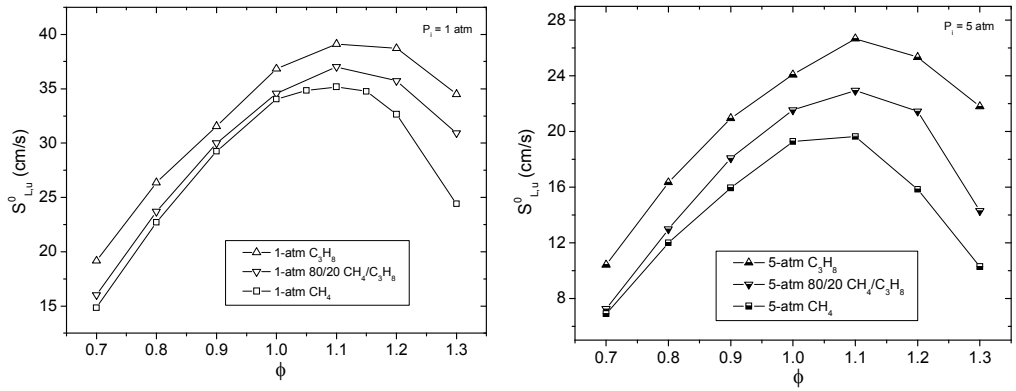

(a) **(b)**

Figure 33 Results for methane/propane laminar flame speeds. (a) Flame speed for 1-atm C_3H_8, 80/20 CH_4/C_3H_8, and CH_4, (b) Flame speed for 5-atm C_3H_8, 80/20 CH_4/C_3H_8, and CH_4.

Similarly to Figure 32, Figure 33 also shows that an increase in the concentration of the faster burning fuel results in a faster flame speed. Good qualitative agreement is seen between Figure 33a and Figure 33b, as for both initial pressures, similar behavior is seen.

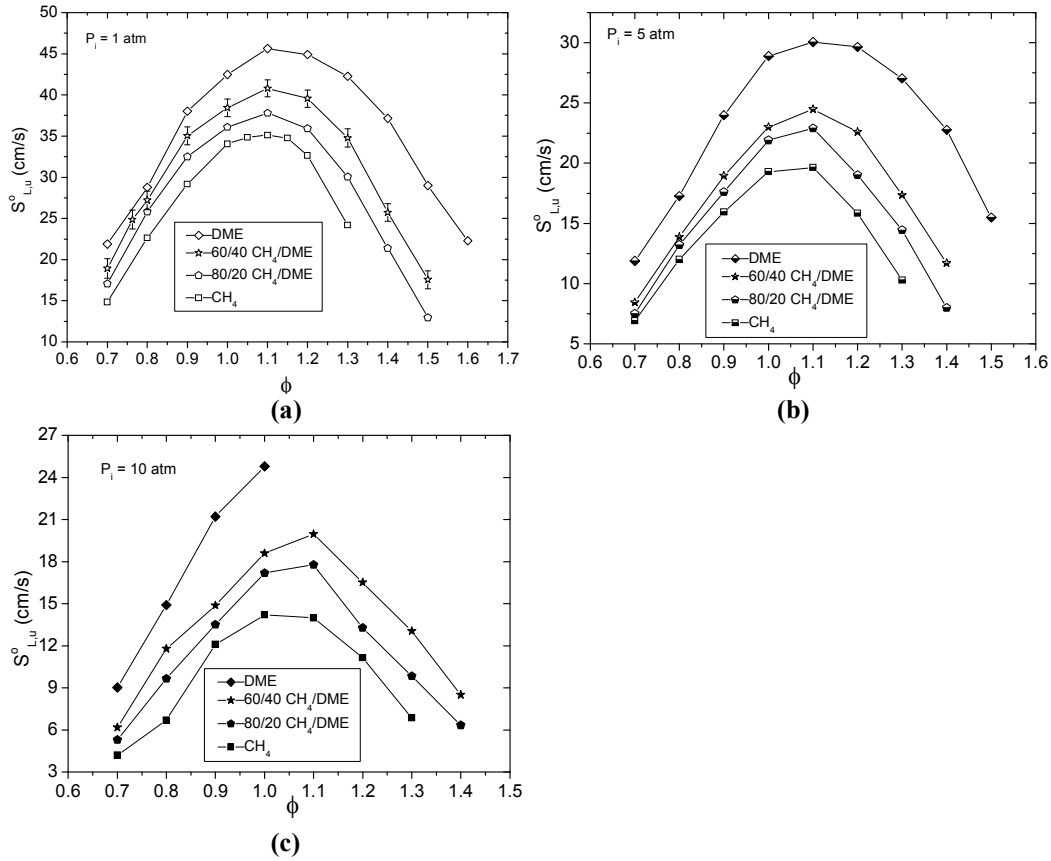

Figure 34 Results for methane/DME laminar flame speeds. (a) Flame speed for 1-atm CH_3OCH_3, 60/40 CH_4/CH_3OCH_3, 80/20 CH_4/CH_3OCH_3 and CH_4, (b) Flame speed for 5-atm CH_3OCH_3, 60/40 CH_4/CH_3OCH_3, 80/20 CH_4/CH_3OCH_3 and CH_4, (c) Flame speed for 10-atm CH_3OCH_3, 60/40 CH_4/CH_3OCH_3, 80/20 CH_4/CH_3OCH_3 and CH_4.

Figure 34 also shows that an increase in the faster-burning fuel increases the laminar burning velocity. This effect is expected, and the same behavior is seen for Figures 32-34. These plots were created, in part, to show the internal consistency of the data since there were no other experimental data available in the literature. Figures 32-34 would allow one to easily see inconsistencies in the data since it was expected that the mixture containing more of the faster-burning fuel would have a faster mass burning flux ($\dot{m}" = \rho_u S_{L,u}^o$) and therefore faster laminar burning velocity since the density does not change much as the fuels are mixed.

5.4 Critical Radius, Lewis Number Trends, and Markstein Lengths

In this study, flame acceleration due to instabilities was seen for initial pressures of 5 and 10 atm. At 5-atm initial pressure, propane exhibited instabilities for equivalence ratios greater than 0.8, DME showed instabilities for equivalence ratios greater than 0.7, and pure methane and pure ethane displayed instabilities for the entire range of equivalence ratios investigated. Instabilities were seen for all fuels in this study at an initial pressure of 10 atm, and this limited the range of useable data for DME and propane. As mentioned previously, a flame was considered unstable when it could no longer be characterized as a laminar flame, determined by the onset of flame acceleration and shown by the residual method. The dynamics of flame instabilities are coupled with the Lewis number (Law, 1988), so Le for each mixture tested was calculated at 1 atm. Table 3 presents the results of the Le calculations for the pure-fuel and multi-fuel-blend mixtures studied herein.

Table 3 Lewis number results for atmospheric, off-stoichiometric mixtures

ϕ	CH_4	C_2H_6	C_3H_8	DME	60/40 CH_4/C_2H_6	80/20 CH_4/C_2H_6	80/20 CH_4/C_3H_8	60/40 CH_4/DME	80/20 CH_4/DME
0.7	0.98	1.41	1.81	1.57	1.20	1.10	1.25	1.36	1.21
0.8	0.98	1.40	1.79	1.56	1.19	1.10	1.25	1.36	1.21
0.9	0.98	1.40	1.78	1.54	1.19	1.10	1.25	1.35	1.21
1.1	1.05	0.99	0.98	0.92	1.02	1.03	1.02	0.99	1.02
1.2	1.05	0.98	0.97	0.91	1.01	1.03	1.02	0.99	1.02
1.3	1.05	0.98	0.96	0.90	1.01	1.03	1.02	0.98	1.01

Table 3 shows that for a blend of fuels, the blend's Le falls between the values of the pure fuels. This result suggests that the blended fuel's reaction to instabilities should fall between the pure fuels' response to instabilities. From the experimental data, the blended fuels typically showed a reduction in the onset of instabilities and acceleration due to instabilities when compared to the pure fuels. Tables 4 and 5 show the critical radii for methane, ethane, propane, DME, and fuel blends at initial pressures of 5 and 10 atm, where (—) denotes that the flame did not become unstable, and NA indicates that there was no experiment performed for that condition.

Table 4 Critical radii (cm) for CH_4, C_2H_6, C_3H_8, DME, and selected binary blends at 5-atm initial pressure, where (--) denotes that the flame did not become unstable

ϕ	CH_4	C_2H_6	C_3H_8	DME	80/20 CH_4/C_3H_8	60/40 CH_4/DME	80/20 CH_4/DME
0.7	3.98	4.39	--	--	--	--	--
0.8	4.29	3.77	--	4.89	--	--	--
0.9	4.19	3.39	4.56	4.75	--	4.83	--
1	3.30	3.74	4.38	4.23	--	4.65	--
1.1	3.57	3.23	3.82	3.72	4.08	4.16	--
1.2	4.40	3.19	3.65	3.17	--	4.75	--
1.3	4.52	2.97	3.17	2.77	--	--	--

Table 5 Critical radii (cm) for methane, ethane, and methane/ethane blends at an initial pressure of 10 atm

ϕ	CH_4	C_2H_6	80/20 CH_4/C_2H_6	60/40 CH_4/C_2H_6
0.7	--	--	--	--
0.8	3.25	NA	3.90	4.50
0.9	3.13	3.13	3.43	3.91
1	3.30	2.42	3.38	3.68
1.1	3.42	2.54	3.85	3.49
1.2	4.16	2.23	4.36	4.09
1.3	4.54	--	--	--

Tables 4 and 5 show that the blended fuels were more stable than the pure-fuel constituents alone due to their typically larger critical radii. This trend reflects the results that the blended-fuels' Le were typically closer to unity than either of the pure fuels in the mixture. For example, at an initial pressure of 10 atm, pure methane became unstable during flame propagation for equivalence ratios greater than 0.7, while ethane was unstable at the early stages of flame propagation for equivalence ratios from 0.9 to 1.2. However, for both 60/40 and 80/20 blends of methane and ethane, the flame was stable for equivalence ratios of 0.7 and 1.3. In addition, these fuel blends became unstable at a larger flame radius. The results in Table 4 show an even more dramatic improvement in stability for a fuel blend compared to its pure-fuel constituents. The 80/20 methane/propane blend at an initial pressure of 5 atm became unstable for only one equivalence ratio, while the pure methane became unstable for every equivalence ratio, and the pure propane was unstable for equivalence ratios greater than 0.9. Also shown in Table 4, the CH_4/DME fuel

blends exhibited less instability than the pure fuels that compose them, and the critical radii were less than both of the pure fuels investigated except for the equivalence ratio of 1.1.

However, the critical radius values do not exactly match the Le trends. In part, this could be due to the change in the flame thickness when the two pure fuels are blended. If the flame thickness were to increase by a large amount, then the hydrodynamic instabilities would be decreased. In this study, the flame thicknesses of the blends did not vary by a large amount when compared to the fuels that composed them. For example, at 1-atm initial pressure and an equivalence ratio of 0.8, pure DME has a flame thickness of 0.41 mm, CH_4 has a flame thickness of 0.55 mm, and the 60/40 CH_4/DME blend has a flame thickness of 0.49 mm. Similarly, for an equivalence ratio of 0.9 at 5-atm initial pressure, DME has a flame thickness of 0.11 mm, CH_4 has a flame thickness of 0.16 mm, and the 60/40 CH_4/DME blend has a thickness of 0.13 mm. Therefore, it is not expected that the change in flame thickness will play a large role in flame stability for this study.

This discrepancy between the Le trends and critical radii could also be due to the small change in Le for methane when compared to C_2H_6, C_3H_8, and DME. The Le for methane does not change by a large amount as the equivalence ratio changes, as shown in Table 3, so its blends aren't expected to show large stability changes in response to varying the equivalence ratio. A fuel displaying a larger change in Le that followed the trend of CH_4, from below unity to above unity as equivalence ratio increases, would show more definitive trends in the critical radius in its pure form and in blends with other fuels displaying opposite trends in Le. The 5-atm data were used for some of the fuels because the 10-atm data did not clearly show trends relating the two. The authors feel that the transition from a laminar flame, marked by flame acceleration, occurs faster than the framing rate of the camera used in this study. Therefore, there is a sudden jump in the residuals plot, Figure 20, when the flame becomes unstable for the 10-atm cases, and the radius exactly where this change occurs is not able to be accurately defined. Defining this radius is possible for the 5-atm data because, even though the flame itself is faster, the transition to an unstable flame occurs more slowly. In addition, 10-atm pure DME became unstable very early in its propagation,

and it was not possible to solve for the flame parameters for any of the fuel rich experiments due to the very small critical radii.

Hybrid responses were seen in the Markstein lengths for fuel blends as well. Figure 35 shows the experimentally determined Markstein lengths for atmospheric methane, ethane, propane, methane/ethane blends, and the methane/propane blend. Figure 35a shows that the Markstein lengths for both methane/ethane blends typically fall between the Markstein lengths for the pure fuels. This result shows that the blends' response to stretch is a mixture of both the pure methane response to stretch and the pure ethane response to stretch. This statement is further strengthened by the previously mentioned results that the fuel blends exhibited fewer instabilities compared to the pure fuels that compose the blends. Additionally, Figure 35a shows that the methane/ethane blends' sensitivity to stretch is almost constant throughout the tested equivalence ratios. Figure 35b, presenting the results for C_3H_8 and its blends, shows again that the multi-fuel-blend mixtures exhibit a combination of the pure fuels' response to stretch. The Markstein lengths found in this study compare favorably to previous work by Gu et al. (2000), Rozenchan et al. (2002), and Tahtouh et al. (2009). Figure 35c shows the atmospheric-methane Markstein length results from this study in comparison to previous studies.

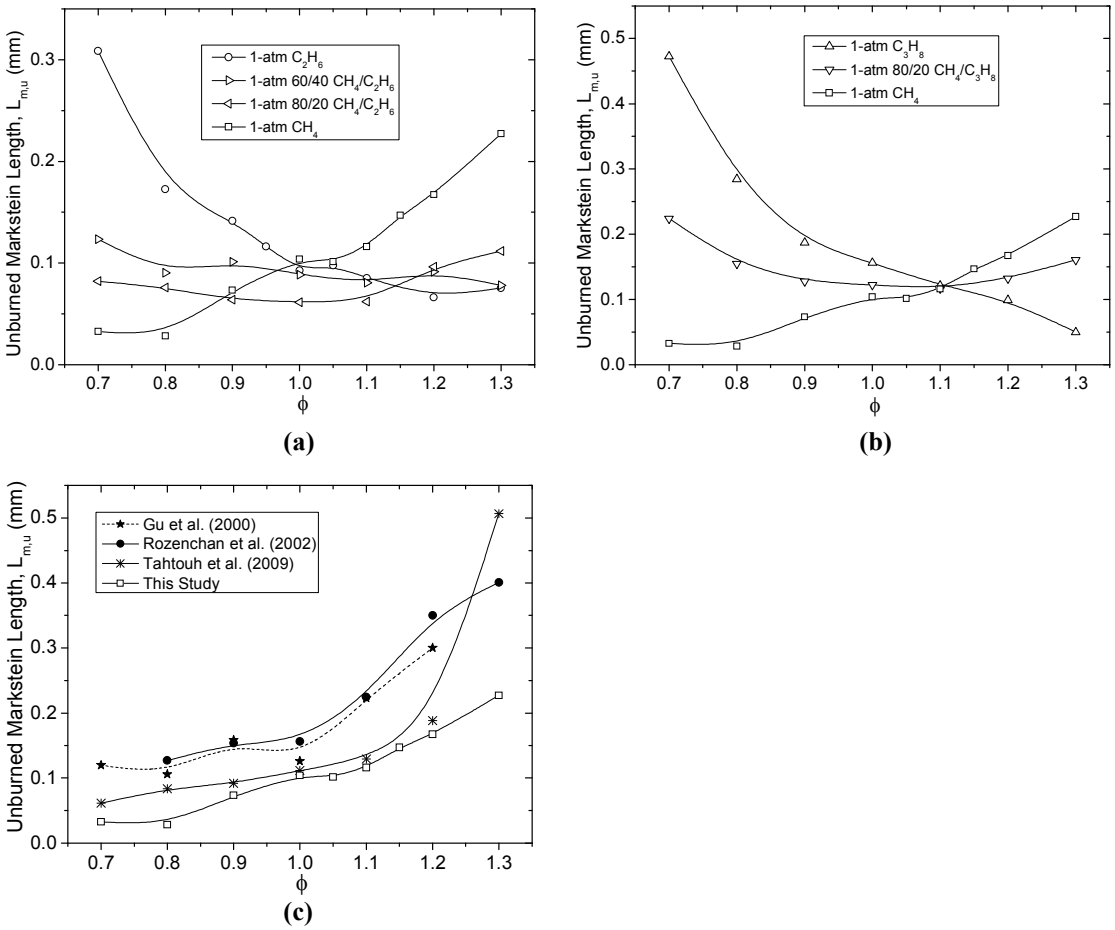

Figure 35 Markstein lengths for various blends. (a) Markstein lengths of atmospheric ethane, 60/40 CH_4/C_2H_6, 80/20 CH_4/C_2H_6, and CH_4, (b) Markstein lengths of atmospheric propane, 80/20 CH_4/C_3H_8, and CH_4, (c) Markstein lengths of atmospheric CH_4 compared to previous experimental work.

Figure 36 shows Markstein lengths of pure CH_4, DME, 60/40 CH_4/DME, and 80/20 CH_4/DME as a function of equivalence ratio at an initial pressure of 1 atm. The lines in Figure 36 represent no additional data or model calculation, but are provided to clearly show trends and guide the eye.

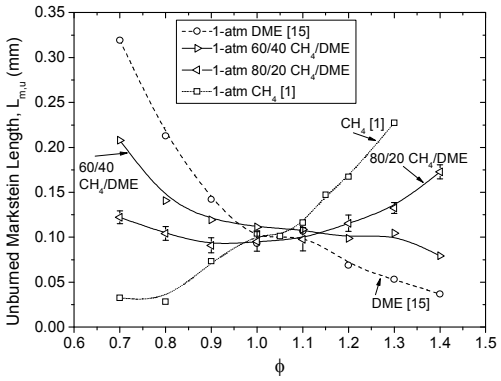

Figure 36 Markstein lengths for DME, 60/40 CH_4/DME, 80/20 CH_4/DME, and CH_4 at 1 atm.

Figure 36 shows that a small amount of DME added to CH_4 results in a large increase in the Markstein length. This increase was also observed by Chen et al. (2007). The dependence of the Markstein length on equivalence ratio for the fuels studied is expected, as shown from the Le trends. For the Markstein length, a positive dependence on equivalence ratio suggests that the Le depends positively on the equivalence ratio and vice versa (Burke et al., 2009; Joulin and Mitani, 1981). This trend is seen for all the fuels studied, but it is not as clear for the 80/20 CH_4/DME blend due to the small change in Le and Markstein length as equivalence ratio changes.

CHAPTER VI

CONCLUSIONS

This thesis showed experimental results for binary blends of CH_4/C_2H_6, CH_4/C_3H_8, and CH_4/CH_3OCH_3 at initial pressures of 1, 5, and 10 atm, with volumetric fractions of CH_4 ranging from 60% to 80%. The experiments were performed in a constant-volume vessel with optical access to measure the propagation of the flame as a function of time. A Z-type schlieren setup was used in conjunction with a high-speed camera to visualize the flame front and image-tracking software using a best-fit circle around the flame was used to find the flame radius as a function of time. Flame stretch was then taken into account using a linear relation between the flame stretch and the flame speed.

The pure fuel results were also shown for comparison, though they have been treated at length elsewhere (de Vries 2009; de Vries et al. 2010). The experimental data were also compared to a modified chemical kinetics model and other available models. The C4 model agreement with the data was excellent in all cases. The C4 model has been proven increasingly robust, agreeing with laminar flame speed data ranging from pure and blended C1-C3 alkanes to pure DME and its blends with CH_4. In addition, the C4 model has been historically proven to agree extremely well with high-pressure shock-tube data at varying temperatures and RCM low-temperature data. A rigorous uncertainty analysis was performed, revealing an experimental uncertainty ranging from 0.3 cm/s to 3.5 cm/s of the true value of the laminar flame speed. Atmospheric Markstein lengths were also presented for all fuels studied. Finally, flame stability, determined by the critical radius, was experimentally shown to follow the Le trends of the mixture. At an initial pressure of 5 atm, all the fuels studied displayed decreasing critical radii as the Le decreased below unity and increasing critical radii as Le increased above unity. This behavior was especially evident in the fuel blends when comparing the 5-atm 60% CH_4/40% DME, where the Le decreased to below unity, to the 80% CH_4/20% DME, where the Le did not fall below unity.

REFERENCES

Aldredge, R.C., and Killingsworth, N.J. 2004. Experimental evaluations of Markstein-number influence on thermoacoustic instability. *Combustion and Flame*, **137**, 178-197.

Aung, K.T., Hassan, M.I., and Faeth, G.M. 1997. Flame stretch interactions of laminar premixed hydrogen/air flames at normal temperature and pressure. *Combustion and Flame*, **109**, 1-24.

Badin, E.J., Stuart, J.G., and Pease, R.N. 1949. Burning velocities of butadiene-1, 3 with nitrogen-oxygen and helium-oxygen mixtures. *Journal of Chemical Physics*, **17**, 314-316.

Bosschaart, K.J. and de Goey, L.P.H. 2004. The laminar burning velocity of flames propagating in mixtures of hydrocarbons and air measured with the heat flux method. *Combustion and Flame*, **136**, 261-269.

Bourque, G., Healy, D., Curran, H., Zinner, C., Kalitan, D., de Vries, J., Aul, C., and Petersen, E. 2008. Ignition and flame speed kinetics of two natural gas blends with higher levels of hydrocarbons. 2008 ASME Turbo Expo, Berlin, Germany, June 9-13, Paper # GT2008-41344.

Bowman, C.T., Hanson, R.K., Davidson, D.F., Gardiner, W.C. Jr., Lissianski, V., Smith, G.P., Golden, D.M., Frenklach, M., and Goldenberg, M. 1995. GRI 2.11 Mechanism. http://www.me.berkeley.edu/gri_mech/

Bradley, D., Hicks, R.A., Lawes, M., Sheppard, C.G.W., and Woolley, R. 1998. The measurement of laminar burning velocities and Markstein numbers for iso-octane-air and iso-octane-n-heptane-air mixtures at elevated temperatures and pressures in an explosion bomb. *Combustion and Flame*, **115**, 126-144.

Brown, M.J., McLean, I.C., Smith, D.B., and Taylor, S.C. 1996. Markstein lengths of CO/H_2/air flames, using expanding spherical flames. *Proceedings of the Combustion Institute*, **26**, 875-881.

CHEMKIN-PRO. (2008). Reaction Design, San Diego, CA.

Chen, Z., Qin, X., Ju, Y., Zhao, Z., Chaos, M., and Dryer, F.L. 2007. High temperature ignition and combustion enhancement by dimethyl ether addition to methane-air mixtures. *Proceedings of the Combustion Institute*, **31**, 1215-1222.

Chen, Z., Wei, L., Huang, Z., Miao, H., Wang, X, and Jiang, D. 2009. Measurement of laminar burning velocities of dimethyl ether-air premixed mixtures with N_2 and CO_2 dilution. *Energy Fuels*, **23**, 735-739.

Clingman, W.H., Brokaw, R.S., and Pease, R.N. 1953. Burning velocities of methane with nitrogen-oxygen, argon-oxygen, and helium-oxygen mixtures. *Proceedings of the Combustion Institute*, **4**, 310-313.

Curran, H.J., Fischer, S.L., and Dryer, F.L. 2000. The reaction kinetics of dimethyl ether. II: Low-temperature oxidation in flow reactors. *International Journal of Chemical Kinetics*, **32**, 741-759.

Daly, C.A., Simmie, J.M., Wurmel, J., Djebaili, N., and Paillard, C. 2001. Burning velocities of dimethyl ether and air. *Combustion and Flame*, **125**, 1329 – 1340.

de Vries, J. 2010. A study on spherically expanding flame speeds of methane, ethane, and methane/ethane mixtures at elevated pressures. Doctoral Dissertation, Texas A&M University, College Station, TX, USA.

de Vries, J., Lowry, W.B., Serinyel, Z., Curran, H.J., and Petersen, E.L. 2010. Laminar flame speed measurements of dimethyl ether in air at pressures up to 10 atm. *Fuel*, doi:10.1016/j.fuel.2010.07.040

Dowdy, D.R., Smith, D.B., Taylor, S.C., and Williams, A. 1990. The use of expanding spherical flames to determine burning velocities and stretch effects in hydrogen/air mixtures. *Proceedings of the Combustion Institute*, **23**, 325-332.

Dyakov, I.V., De Ruyck, J., and Konnov, A.A. 2007. Probe sampling measurements and modeling of nitric oxide formation in ethane + air flames. *Fuel*, **86**, 98-105.

Dyakov, I.V., Konnov, A.A., De Ruyck, J., Bosschaart, K.J., Brock, E.C.M., and De Goey, L.P.H. 2001. Measurement of adiabatic burning velocity in methane-oxygen-nitrogen mixtures. *Combustion Science and Technology*, **172**, 81-96.

Egolfopoulos, F. N., Wang, Hai, Hanson, R. K., Davidson, D. F., Bowman, C. T., Pitsch, H., Law, C. K., Cernansky, N. P., Miller, D. L., Tsang, W., Lindstedt, R. P., and Violi, A. 2009. JetSurF version 1.0 - A working model for n-alkane combustion. http://melchior.usc.edu/JetSurF/

Fischer, S.L., Dryer, F.L., and Curran, H.J. 2000. The reaction kinetics of dimethyl ether. I: High-temperature pyrolysis and oxidation in flow reactors. *International Journal of Chemical Kinetics*, **32**, 713-740.

Gibbs, G.J. and Calcote, H.F. 1959. Effect of molecular structure on burning velocity. *Journal of Chemical and Engineering Data*, **4**, 226-237.

Gu, X.J., Haq, M.Z., Lawes, M., and Woolley, R. 2000. Laminar burning velocity and Markstein lengths of methane-air mixtures. *Combustion and Flame*, **121**, 41-58.

Hassan, M.I., Aung, K.T., and Faeth, G.M. 1998a. Measured and predicted properties of laminar premixed methane/air flames at various pressures. *Combustion and Flame*, **115**, 539-550.

Hassan, M.I., Aung, K.T., Kwon, O.C., and Faeth, G.M. 1998b. Properties of laminar premixed hydrocarbon/air flames at various pressures. *Journal of Propulsion and Power*, **14**, 479-488.

Healy, D., Curran, H.J., Dooley, S., Simmie, J.M., Kalitan, D.M., Petersen, E.L., and Bourque, G. 2008a. Methane/propane mixture oxidation at high pressures and at high, intermediate and low temperatures. *Combustion and Flame*, **155**, 451-461.

Healy, D., Curran, H.J., Simmie, J.M., Kalitan, D.M., Zinner, C.M., Barrett, A.B., Petersen, E.L., and Bourque, G. 2008b. Methane/ethane/propane mixture oxidation at high pressures and at high, intermediate and low temperatures. *Combustion and Flame*, **155**, 441-448.

Healy, D., Donato, N.S., Aul, C.J., Petersen, E.L., Zinner, C.M., Bourque, G., and Curran, H.J. 2010a. Isobutane ignition delay time measurements at high pressure and detailed chemical kinetic simulations. *Combustion and Flame*, **157**, 1540-1551.

Healy, D., Donato, N.S., Aul, C.J., Petersen, E.L., Zinner, C.M., Bourque, G., and Curran, H.J. 2010b. n-Butane: Ignition delay measurements at high pressure and detailed chemical kinetic simulations. *Combustion and Flame*, **157**, 1526-1539.

Huang, Z., Wang, Q., Yu, J., Zhang, Y., Zeng, K. Miao, H., and Jiang, D. 2007. Measurement of laminar burning velocity of dimethyl ether-air premixed mixtures. *Fuel*, **86**, 2360-2366.

Joulin, G. and Mitani, T. 1981. Linear stability analysis of two reactant flames. *Combustion and Flame*, **40**, 235-246.

Jomaas, G., Zheng, X.L., Zhu, D.L., and Law, C.K. 2005. Experimental determination of counterflow ignition temperatures and laminar flame speeds of C2-C3 hydrocarbons at atmospheric and elevated pressures. *Proceedings of the Combustion Institute,* **30**, 193-200.

Kee, R.J., Dixon-Lewis, G., Warnatz, J., Coltrin, M.E., Miller, J.A., and Moffat, H.K. 1986. A Fortran computer code package for the evaluation of gas-phase, multi-component transport properties. *Sandia National Laboratories Report* SAND86-8246.

Konnov, A.A., Dyakov, I.V., and De Ruyck, J. 2003. Measurement of adiabatic burning velocity in ethane-oxygen-nitrogen and in ethane-oxygen-argon mixtures. *Experimental Thermal Fluid Science*, **27**, 379-384.

Law, C.K. 1988. Dynamics of stretched flames. *Proceedings of the Combustion Institute*, **22**, 1381-1402.

Law, C.K. 2006. *Combustion Physics*, 1st ed. Cambridge University Press, New York, 396-471.

Law, C.K., and Kwon, O.C. 2004. Effects of hydrocarbon substitution on atmospheric hydrogen-air flame propagation. *International Journal of Hydrogen Energy,* **29**, 867-879.

Lieuwen, T.C. and Yang, V. 2005. *Combustion Instabilities in Gas Turbine Engines: Operational Experience, Fundamental Mechanisms, and Modeling*. AIAA, Danvers, MA, 2005.

Liss, W.E., Thrasher, W.H., Steinmetz, G.F., Chowdiah, P., and Attari, A. 1992. Variability of natural gas composition in select major metropolitan areas of the United States. Report# GRI290123, Gas Research Institute, Chicago, IL.

Lowry, W.B., de Vries, J., Krejci, M., Petersen, E., Serinyel, Z., Metcalfe, W.K., Curran, H.J., and Bourque, G. 2010a. Laminar flame speed measurements and modeling of pure alkanes and alkane blends at elevated pressures. 2010 ASME Turbo Expo, Glasgow, Scotland, June 14-18, Paper # GT2010-23050.

Lowry, W.B., Serinyel, Z., Krejci, M.C., Curran, H.J., Bourque, G., and Petersen, E.L. 2010b. Effect of methane-dimethyl ether fuel blends on flame stability, laminar flame speed, and Marksetin length. *Proceedings of the Combustion Institute*, **33**, doi:10.1016/j.proci.2010.05.042.

Markstein, G.H. 1964. *Non-Steady Flame Propagation*, Pergamon, New York.

Metghalchi, M. and Keck, J.C. 1980. Laminar burning velocity of propane-air mixtures at high temperature and pressure. *Combustion and Flame*, **38**, 143-154.

Miller, J.A. and Klippenstein, S.J. 2004. The H + C_2H_2(+M) ↔ C_2H_3(+M) and H + C_2H_2(+M) ↔ C_2H_5(+M) reactions: Electronic structure, variational transistion-state theory, and solutions to a two-dimensional master equation. *Physical Chemistry Chemical Physics*, **6**, 1192-1202.

Moffat, R.J. 1988. Describing uncertainties in experimental results. *Experimental Thermal and Fluid Science*, **1**, 3-17.

Natarajan, J., Lieuwen, T., and Seitzman, J. 2007. Laminar flame speeds of H_2/CO mixtures: Effect of CO_2 dilution, preheat temperature, and pressure. *Combustion and Flame*, **151**, 104-119.

O'Conaire, M., Curran, H.J., Simmie, J.M., Pitz, W.J., and Westbrook, C.K. 2004. A comprehensive modeling study of hydrogen oxidation. *International Journal of Chemical Kinetics*, **36**, 603-622.

Petersen, E.L., Kalitan, D.M., Simmons, S., Bourque, G., Curran, H.J., and Simmie, J.M. 2007. Methane/propane oxidation at high pressures: Experimental and detailed chemical kinetic modeling. *Proceedings of the Combustion Institute*, **31**, 447-454.

Qin, X. and Ju, Y. 2005. Measurements of burning velocities of dimethyl ether and air premixed flames at elevated pressures. *Proceedings of the Combustion Institute*, **30**, 233-240.

Reynolds, W.C. 1986. The element potential method for chemical equilibrium analysis: Implementation in the interactive program STANJAN. Technical Report, Department of Mechanical Engineering, Stanford University, Palo Alto, CA.

Rozenchan, G., Zhu, D.L., Law, C.K., and Tse, S.D. 2002. Outward propagation, burning velocities, and chemical effects of methane flames up to 60 atm. *Proceedings of the Combustion Institute*, **29**, 1461-1469.

San Diego Mechanism 2005. *2005/12/01*, available at http://maeweb.ucsd.edu/~combustion/cermech/ (accessed March 2010)

Settles, G.S. 2006. *Schlieren and shadowgraph techniques: visualizing phenomena in transparent media*, Springer, Heidelberg, Germany.

Shakarji, C.M. 1998. Least-squares fitting algorithms of the NIST algorithm testing system. *Journal of Research of the National Institute of Standards and Technology*, **103**, 633-641.

Smith, G.P., Golden, D.M., Frenklach, M., Moriarty, N.W., Eiteneer, B., Goldenberg, M., Bowman, C.T., Hanson, R.K., Song, S., Gardiner, W.C. Jr., Lissianski, V.V., and Qin, Z. 1999. http://www.me.berkeley.edu/gri_mech/ (accessed March 2010)

Sun, C.J., Sung, C.J., He, L., and Law, C.K. 1999. Dynamics of weakly stretched flames: Quantitative description and extraction of global flame parameters. *Combustion and Flame,* **118**, 108-128.

Sung, C.J. and Law, C.K. 1998. Dominant chemistry and physical factors affecting NO formation and control in oxy-fuel burning. *Proceedings of the Combustion Institute*, **27**, 1411-1418.

Tahtouh, T., Halter, F., and Mounaim-Rousselle, C. 2009. Measurement of laminar burning speeds and Markstein lengths using a novel methodology. *Combustion and Flame,* **156**, 1735-1743.

Troe, J. 1983. Theory of the thermal unimolecular reactions in the fall-off range. I. Strong collision rate constants. *Berichte der Bunsengesellschaft für physikalische Chemie*, **87**, 161-169.

Tsuji, H. and Yamaoka, I. 1982. Structure and extinction of near-limit flames in a stagnation flow. *Proceedings of the Combustion Institute*, **19**, 1533-1540.

Turns, S.R. 2000. *An Introduction to Combustion: Concepts and Applications*, 2nd ed., McGraw Hill, Boston, 253-283.

Vagelopoulos, C.M. and Egolfopoulos, F.N. 1998. Direct experimental determination of laminar flame speeds. *Proceedings of the Combustion Institute,* **27**, 513-519.

Van Maaren, A. and de Goey, L.P.H. 1994. Stretch and the adiabatic burning velocity of methane- and propane-air flames. *Combustion Science and Technology*, **102**, 309-314.

Zhao, Z., Kazakov, A., Li, J., and Dryer, F.L. 2004. The initial temperature and N_2 dilution effect on the laminar flame speed of propane/air. *Combustion Science and Technology,* **176**, 1705-1723.

APPENDIX

Table A1 Experimental results for methane at initial pressures of 1, 5, and 10 atm

CH_4 (%)	C_2H_6 (%)	C_3H_8 (%)	ϕ	$S^0_{L,u}$ (cm/s)	L_m (cm)	σ	T_u (K)	P_i (atm)
100	0	0	0.7	14.85	0.0033	6.18	293.6	1
100	0	0	0.8	22.63	0.0028	6.72	293.6	1
100	0	0	0.9	29.17	0.0073	7.20	294.3	1
100	0	0	1.0	33.83	0.0121	7.52	296.0	1
100	0	0	1.05	34.85	0.0101	7.60	294.6	1
100	0	0	1.1	35.12	0.0116	7.58	294.1	1
100	0	0	1.15	34.75	0.0147	7.51	293.8	1
100	0	0	1.2	32.64	0.0167	7.44	294.2	1
100	0	0	1.3	24.18	0.0227	7.29	293.5	1
100	0	0	0.70	6.91	-0.00071	6.188	294.0	5
100	0	0	0.80	12.00	0.00398	6.739	295.0	5
100	0	0	0.90	15.95	0.00147	7.240	295.0	5
100	0	0	1.00	19.28	0.00336	7.629	295.0	5
100	0	0	1.10	19.64	0.00583	7.610	291.0	5
100	0	0	1.20	15.84	0.00591	7.454	293.0	5
100	0	0	1.30	10.29	0.01215	7.293	300.0	5
100	0	0	0.70	4.21	-0.00867	6.190	292.0	10
100	0	0	0.80	6.71	-0.00009	6.743	295.0	10
100	0	0	0.90	12.09	0.00186	7.253	292.0	10
100	0	0	1.00	14.20	0.00239	7.659	292.0	10
100	0	0	1.10	13.99	0.00198	7.618	292.0	10
100	0	0	1.20	11.14	0.00375	7.458	292.0	10
100	0	0	1.30	6.86	0.00772	7.295	294.0	10

Table A2 Experimental results for ethane at initial pressures of 1, 5, and 10 atm

CH_4 (%)	C_2H_6 (%)	C_3H_8 (%)	ϕ	$S^0_{L,u}$ (cm/s)	L_m (cm)	σ	T_u (K)	P_i (atm)
0	100	0	0.7	21.08	0.0309	6.43	295.0	1
0	100	0	0.8	27.78	0.0173	7.01	295.0	1
0	100	0	0.9	34.51	0.0141	7.52	295.0	1
0	100	0	0.95	36.10	0.0116	7.73	297.0	1
0	100	0	1	37.61	0.0093	7.89	293.1	1
0	100	0	1.05	38.66	0.0098	7.97	294.3	1
0	100	0	1.1	39.07	0.0085	7.98	294.9	1
0	100	0	1.2	37.81	0.0066	7.89	293.5	1
0	100	0	1.3	33.69	0.0075	7.76	295.0	1
0	100	0	0.7	13.39	0.0047	6.44	295.0	5
0	100	0	0.8	18.76	0.0050	7.03	296.0	5
0	100	0	0.9	23.34	0.0012	7.58	294.0	5
0	100	0	1	26.77	0.0025	7.99	294.0	5
0	100	0	1.1	28.36	0.0043	8.04	295.0	5
0	100	0	1.2	27.36	0.0031	7.91	298.0	5
0	100	0	1.3	21.75	0.0027	7.78	295.0	5
0	100	0	0.64	6.99	0.0095	6.06	294.0	10
0	100	0	0.9	20.03	0.0032	7.59	298.0	10
0	100	0	1	23.94	0.0052	8.03	294.0	10
0	100	0	1.1	24.71	0.0023	8.05	293.6	10
0	100	0	1.2	23.71	0.0015	7.92	295.0	10

Table A3 Experimental results for propane at initial pressures of 1 and 5 atm

CH_4 (%)	C_2H_6 (%)	C_3H_8 (%)	ϕ	S_L (cm/s)	L_m (cm)	σ	T_u (K)	P_i (atm)
0	0	100	0.7	19.17	0.0473	6.50	295.0	1
0	0	100	0.8	26.37	0.0285	7.10	291.0	1
0	0	100	0.9	31.55	0.0187	7.63	291.2	1
0	0	100	1	36.84	0.0156	8.00	295.0	1
0	0	100	1.1	39.12	0.0121	8.12	295.6	1
0	0	100	1.2	38.72	0.0099	8.04	294.5	1
0	0	100	1.3	34.51	0.0050	7.92	295.4	1
0	0	100	0.7	10.42	0.0181	6.51	296.0	5
0	0	100	0.8	16.35	0.0080	7.13	295.4	5
0	0	100	0.9	20.95	0.0058	7.68	296.2	5
0	0	100	1	24.10	0.0027	8.12	296.0	5
0	0	100	1.1	26.68	0.0013	8.18	295.4	5
0	0	100	1.2	25.35	0.0012	8.06	296.0	5
0	0	100	1.3	21.81	-0.0002	7.93	297.2	5

Table A4 Experimental results for dimethyl ether at initial pressures of 1, 5 and 10 atm

CH_4 (%)	CH_3OCH_3 (%)	ϕ	$S^0_{L,u}$ (cm/s)	L_m (cm)	σ	T_u (K)	P_i (atm)
0	100	0.7	21.89	0.03191	6.80	295.4	1
0	100	0.8	28.78	0.02127	7.40	296.5	1
0	100	0.9	38.01	0.01419	7.91	295.9	1
0	100	1	42.46	0.00930	8.29	295.9	1
0	100	1.1	45.62	0.01066	8.45	296.0	1
0	100	1.2	44.90	0.00688	8.44	296.8	1
0	100	1.3	42.26	0.00530	8.38	296.9	1
0	100	1.4	37.16	0.00368	8.30	296.9	1
0	100	1.5	28.99	-0.00238	8.22	295.9	1
0	100	1.6	22.29	-0.00309	8.13	296.6	1
0	100	0.7	11.88	0.01055	6.81	292.5	5
0	100	0.8	17.27	0.00240	7.43	294.0	5
0	100	0.9	23.97	0.00541	7.99	295.0	5
0	100	1	28.89	0.00505	8.41	295.0	5
0	100	1.1	30.05	0.00472	8.53	295.8	5
0	100	1.2	29.65	0.00382	8.48	295.2	5
0	100	1.3	27.03	0.00669	8.40	296.0	5
0	100	1.4	22.76	0.00401	8.31	297.5	5
0	100	1.5	15.49	0.00083	8.23	297.0	5
0	100	0.70	9.03	0.00628	6.81	294.1	10
0	100	0.80	14.90	0.00330	7.44	298.1	10
0	100	0.90	21.21	0.00473	8.01	294.0	10
0	100	1.00	24.78	0.00816	8.46	296.8	10

Table A5 Experimental results for 80/20 CH_4/C_2H_6 at initial pressures of 1, 5, and 10 atm

CH_4 (%)	C_2H_6 (%)	C_3H_8 (%)	ϕ	$S^0_{L,u}$ (cm/s)	L_m (cm)	σ	T_u (K)	P_i (atm)
80	20	0	0.7	16.78	0.0082	6.26	291.9	1
80	20	0	0.8	24.79	0.0076	6.81	292.4	1
80	20	0	0.9	30.45	0.0064	7.29	293.3	1
80	20	0	1	34.56	0.0061	7.64	292.4	1
80	20	0	1.1	36.06	0.0062	7.70	293.2	1
80	20	0	1.2	34.27	0.0096	7.57	294.0	1
80	20	0	1.3	27.48	0.0112	7.43	294.3	1
80	20	0	0.7	8.47	0.0046	6.26	292.5	5
80	20	0	0.75	11.01	0.0022	6.55	293.0	5
80	20	0	0.8	13.39	0.0016	6.83	293.0	5
80	20	0	0.9	19.87	0.0023	7.34	293.4	5
80	20	0	1	21.89	0.0030	7.74	295.6	5
80	20	0	1.1	23.17	0.0045	7.74	295.8	5
80	20	0	1.2	20.15	0.0037	7.59	295.8	5
80	20	0	1.3	14.20	0.0037	7.43	292.2	5
80	20	0	0.7	5.46	-0.0102	6.26	294.7	10
80	20	0	0.8	10.37	-0.0001	6.83	294.5	10
80	20	0	0.9	14.26	-0.0010	7.35	295.7	10
80	20	0	1	16.99	0.0002	7.77	295.1	10
80	20	0	1.1	18.26	0.0024	7.74	298.2	10
80	20	0	1.2	13.37	-0.0013	7.59	297.3	10
80	20	0	1.3	8.16	-0.0046	7.44	297.3	10

Table A6 Experimental results for 60/40 CH_4/C_2H_6 at initial pressures of 1, 5, and 10 atm

CH_4 (%)	C_2H_6 (%)	C_3H_8 (%)	ϕ	$S^0_{L,u}$ (cm/s)	L_m (cm)	σ	T_u (K)	P_i (atm)
60	40	0	0.7	18.20	0.0123	6.314	295.0	1
60	40	0	0.8	25.49	0.0090	6.876	294.1	1
60	40	0	0.9	32.00	0.0101	7.368	292.0	1
60	40	0	1	35.77	0.0089	7.723	292.5	1
60	40	0	1.1	37.39	0.0081	7.793	291.7	1
60	40	0	1.2	35.01	0.0091	7.679	291.1	1
60	40	0	1.3	29.06	0.0078	7.537	292.1	1
60	40	0	0.7	9.44	0.0020	6.32	294.2	5
60	40	0	0.8	15.69	0.0031	6.90	296.2	5
60	40	0	0.9	20.96	0.0027	7.42	294.6	5
60	40	0	1	23.70	0.0020	7.82	295.2	5
60	40	0	1.1	25.13	0.0069	7.83	294.2	5
60	40	0	1.2	23.38	0.0059	7.70	295.2	5
60	40	0	1.3	15.55	0.0015	7.55	295.2	5
60	40	0	0.7	7.02	-0.0020	6.32	294.6	10
60	40	0	0.8	12.33	0.0006	6.90	294.8	10
60	40	0	0.9	16.84	0.0034	7.43	296.5	10
60	40	0	1	20.66	0.0040	7.86	293.3	10
60	40	0	1.1	22.04	0.0087	7.84	296.3	10
60	40	0	1.2	19.98	0.0149	7.70	293.5	10
60	40	0	1.25	15.59	0.0053	7.62	293.5	10
60	40	0	1.3	9.79	-0.0020	7.55	292.9	10

Table A7 Experimental results for 80/20 CH_4/C_3H_8 at initial pressures of 1 and 5 atm

CH_4 (%)	C_2H_6 (%)	C_3H_8 (%)	ϕ	S_L (cm/s)	L_m (cm)	σ	T_u (K)	P_i (atm)
80	0	20	0.7	16.02	0.0224	6.30	293.6	1
80	0	20	0.8	23.69	0.0155	6.87	292.6	1
80	0	20	0.9	30.00	0.0128	7.36	291.6	1
80	0	20	1.0	34.58	0.0122	7.71	292.7	1
80	0	20	1.1	37.02	0.0117	7.78	293.7	1
80	0	20	1.2	35.73	0.0132	7.66	292.2	1
80	0	20	1.3	30.93	0.0161	7.52	293.1	1
80	0	20	0.7	7.25	0.0056	6.31	295.1	5
80	0	20	0.8	12.99	0.0018	6.88	295.3	5
80	0	20	0.9	18.08	0.0009	7.41	295.2	5
80	0	20	1.0	21.55	0.0032	7.81	295.1	5
80	0	20	1.1	22.94	0.0014	7.82	293.7	5
80	0	20	1.2	21.45	0.0043	7.68	293.8	5
80	0	20	1.3	14.30	0.0024	7.53	292.8	5

Table A8 Experimental results for 80/20 CH_4/CH_3OCH_3 at initial pressures of 1, 5, and 10 atm

CH_4 (%)	CH_3OCH_3 (%)	ϕ	$S^0_{L,u}$ (cm/s)	L_m (cm)	σ	T_u (K)	P_i (atm)
80	20	0.7	17.10	0.0122	6.35	295.0	1
80	20	0.8	25.80	0.0104	6.91	295.2	1
80	20	0.9	32.51	0.0091	7.39	295.9	1
80	20	1	36.09	0.0095	7.74	296.0	1
80	20	1.1	37.80	0.0098	7.82	294.4	1
80	20	1.2	35.90	0.0116	7.71	295.1	1
80	20	1.3	30.04	0.0133	7.58	295.9	1
80	20	1.4	21.39	0.0173	7.44	294.7	1
80	20	1.5	12.95	0.0259	7.30	295.5	1
80	20	0.7	7.50	0.00009	6.36	292.0	5
80	20	0.8	13.21	0.00368	6.93	292.7	5
80	20	0.9	17.61	0.00081	7.44	293.2	5
80	20	1	21.91	0.00504	7.84	293.1	5
80	20	1.1	22.89	0.00446	7.86	293.9	5
80	20	1.2	19.02	0.00065	7.73	293.8	5
80	20	1.3	14.44	0.00102	7.59	292.9	5
80	20	1.4	8.00	0.00423	7.44	293.6	5
80	20	0.7	5.31	0.0022	6.36	296.3	10
80	20	0.8	9.69	-0.0035	6.93	296.7	10
80	20	0.9	13.52	-0.0007	7.46	292.3	10
80	20	1	17.18	0.0047	7.87	295.6	10
80	20	1.1	17.78	0.0065	7.87	298.3	10
80	20	1.2	13.27	-0.0005	7.73	296.2	10
80	20	1.3	9.84	0.0031	7.59	294.7	10
80	20	1.4	6.34	-0.0021	7.45	294.5	10

Table A9 Experimental results for 60/40 CH_4/CH_3OCH_3 at initial pressures of 1, 5, and 10 atm

CH_4 (%)	CH_3OCH_3 (%)	ϕ	$S^0_{L,u}$ (cm/s)	L_m (cm)	σ	T_u (K)	P_i (atm)
60	40	0.7	18.93	0.02079	6.49	294.5	1
60	40	0.76	24.87	0.01858	6.86	294.2	1
60	40	0.8	27.19	0.01407	7.06	294.1	1
60	40	0.9	35.05	0.01193	7.55	294.1	1
60	40	1	38.43	0.01113	7.91	297.0	1
60	40	1.1	40.79	0.01085	8.02	295.6	1
60	40	1.2	39.55	0.00988	7.94	294.6	1
60	40	1.3	34.77	0.01046	7.83	295.4	1
60	40	1.4	25.73	0.00793	7.70	295.0	1
60	40	1.5	17.56	0.00402	7.58	295.2	1
60	40	0.7	8.44	0.00509	6.50	292.6	5
60	40	0.8	13.87	0.00400	7.08	292.6	5
60	40	0.9	18.95	0.00249	7.61	293.3	5
60	40	1	22.99	0.00424	8.02	292.3	5
60	40	1.1	24.47	0.00684	8.07	294.7	5
60	40	1.2	22.58	0.00193	7.96	292.1	5
60	40	1.3	17.35	0.00271	7.84	292.0	5
60	40	1.4	11.70	0.00067	7.71	292.8	5
60	40	0.7	6.17	0.0052	6.50	289.7	10
60	40	0.8	11.80	0.0056	7.09	297.0	10
60	40	0.9	14.88	0.0014	7.63	293.3	10
60	40	1	18.60	0.0025	8.05	289.6	10
60	40	1.1	19.96	0.0055	8.08	291.3	10
60	40	1.2	16.52	0.0010	7.96	290.5	10
60	40	1.3	13.06	0.0016	7.84	294.5	10
60	40	1.4	8.51	0.0035	7.71	291.7	10

Table A10 Total uncertainty values (cm/s) for all experiments performed, where (--) denotes no experiment performed for that condition

ϕ	CH_4	C_2H_6	60/40 CH_4/C_2H_6	80/20 CH_4/C_2H_6	C_3H_8	80/20 CH_4/C_3H_8	60/40 CH_4/CH_3OCH_3	80/20 CH_4/CH_3OCH_3	DME
1-atm									
0.7	1.53	0.49	3.37	1.89	0.59	0.95	0.69	0.76	1.69
0.8	1.50	0.45	3.36	1.88	0.57	0.93	0.65	0.72	1.68
0.9	1.47	0.39	3.35	1.86	0.53	0.90	0.58	0.66	1.67
1	1.44	0.33	3.34	1.84	0.49	0.86	0.51	0.59	1.65
1.1	1.44	0.30	3.34	1.84	0.47	0.84	0.48	0.57	1.63
1.2	1.49	0.36	3.36	1.86	0.48	0.87	0.55	0.65	1.64
1.3	1.64	0.51	3.39	1.94	0.55	0.96	0.75	0.86	1.67
5-atm									
0.7	1.46	0.41	3.36	1.86	0.53	0.88	0.56	0.63	1.66
0.8	1.47	0.42	3.36	1.86	0.53	0.90	0.58	0.65	1.67
0.9	1.45	0.39	3.36	1.85	0.52	0.89	0.56	0.63	1.66
1	1.44	0.33	3.34	1.84	0.49	0.86	0.50	0.58	1.65
1.1	1.44	0.30	3.34	1.84	0.46	0.85	0.48	0.58	1.63
1.2	1.49	0.37	3.37	1.88	0.49	0.91	0.57	0.67	1.64
1.3	1.54	0.51	3.40	1.92	0.56	0.99	0.71	0.79	1.67
10-atm									
0.7	1.45	0.39	3.35	1.85	--	--	0.52	0.61	1.65
0.8	1.45	--	3.36	1.86	--	--	0.55	0.63	1.66
0.9	1.45	0.38	3.35	1.85	--	--	0.54	0.62	1.66
1	1.43	0.33	3.34	1.84	--	--	0.50	0.58	1.64
1.1	1.44	0.30	3.34	1.84	--	--	0.48	0.58	--
1.2	1.48	0.37	3.37	1.87	--	--	0.56	0.66	--
1.3	1.50	--	3.39	1.90	--	--	0.67	0.74	--

Table A11 Uncertainty on a percentage basis for all the experiments performed, where (--) denotes no experiment performed for that condition

ϕ	CH_4	C_2H_6	60/40 CH_4/C_2H_6	80/20 CH_4/C_2H_6	C_3H_8	80/20 CH_4/C_3H_8	60/40 CH_4/CH_3OCH_3	80/20 CH_4/CH_3OCH_3	CH_3OCH_3
1-atm									
0.7	10.29%	2.30%	18.53%	11.29%	3.09%	5.96%	3.66%	4.42%	7.74%
0.8	6.64%	1.62%	13.20%	7.58%	2.16%	3.94%	2.39%	2.77%	5.85%
0.9	5.04%	1.14%	10.48%	6.11%	1.69%	3.00%	1.67%	2.02%	4.39%
1	4.26%	0.89%	9.35%	5.33%	1.34%	2.50%	1.33%	1.64%	3.88%
1.1	4.09%	0.78%	8.94%	5.09%	1.19%	2.28%	1.17%	1.51%	3.58%
1.2	4.57%	0.95%	9.58%	5.44%	1.24%	2.42%	1.38%	1.81%	3.64%
1.3	6.78%	1.53%	11.68%	7.06%	1.61%	3.11%	2.16%	2.86%	3.94%
5-atm									
0.7	21.10%	3.09%	35.54%	21.92%	5.05%	12.18%	6.58%	8.44%	13.99%
0.8	12.21%	2.22%	21.42%	13.92%	3.26%	6.95%	4.16%	4.93%	9.64%
0.9	9.12%	1.66%	16.01%	9.34%	2.47%	4.94%	2.93%	3.58%	6.92%
1	7.44%	1.24%	14.11%	8.40%	2.02%	3.97%	2.18%	2.65%	5.70%
1.1	7.34%	1.07%	13.31%	7.94%	1.74%	3.69%	1.96%	2.53%	5.43%
1.2	9.38%	1.35%	14.40%	9.32%	1.92%	4.23%	2.51%	3.53%	5.52%
1.3	14.93%	2.33%	21.84%	13.53%	2.57%	6.95%	4.08%	5.47%	6.18%
10-atm									
0.7	34.37%	3.90%	47.73%	33.89%	--	--	8.49%	11.44%	18.29%
0.8	21.67%	--	27.23%	17.91%	--	--	4.67%	6.50%	11.13%
0.9	11.99%	1.90%	19.92%	12.98%	--	--	3.64%	4.57%	7.80%
1	10.10%	1.38%	16.19%	10.82%	--	--	2.67%	3.36%	6.63%
1.1	10.30%	1.23%	15.17%	10.09%	--	--	2.41%	3.26%	--
1.2	13.24%	1.55%	16.85%	14.02%	--	--	3.38%	4.98%	--
1.3	21.88%	--	34.62%	23.31%	--	--	5.11%	7.52%	--

Table A12 Original test matrix for atmospheric 60/40 CH_4/CH_3OCH_3 mixture, with pressures in Torr

ϕ	CH_4	CH_3OCH_3	O_2	N_2
0.7	26.3	43.9	194.3	760
0.8	29.8	49.7	199.0	760
0.9	33.3	55.5	203.5	760
1	36.7	61.2	208.0	760
1.1	40.1	66.8	212.4	760
1.2	43.3	72.2	216.7	760
1.3	46.6	77.6	221.0	760
1.4	49.8	83.0	225.2	760
1.5	52.9	88.2	229.3	760

Table A13 Uncertainties in ϕ and pressure for atmospheric 60/40 CH_4/CH_3OCH_3 mixture, with pressures in Torr unless otherwise noted

Original ϕ	CH_4	CH_3OCH_3	O_2	N_2	New ϕ	Uncertainty in ϕ	Uncertainty in Total Pressure (atm)
0.7	26.26	43.77	194.81	761.9	0.695	0.0045	0.0025
0.8	29.77	49.61	199.45	761.9	0.795	0.0053	0.0025
0.9	33.22	55.36	204.01	761.9	0.894	0.0062	0.0025
1	36.61	61.02	208.50	761.9	0.993	0.0071	0.0025
1.1	39.95	66.58	212.92	761.9	1.092	0.0080	0.0025
1.2	43.24	72.06	217.27	761.9	1.191	0.0090	0.0025
1.3	46.47	77.45	221.55	761.9	1.290	0.0100	0.0025
1.4	49.66	82.76	225.77	761.9	1.389	0.0110	0.0025
1.5	52.79	87.99	229.91	761.9	1.488	0.0121	0.0025

Example chemical kinetics file

```
elements
c h n o ar he
!to modify
end
species
h          h2         o          o2         oh
h2o        n2         ho2        h2o2       ar
co         co2        ch2o       hco        ho2cho
o2cho      hocho      ocho       hoch2o2h   hoch2o2
och2o2h    hoch2o     ch3oh      ch2oh      ch3o
ch3o2h     ch3o2      ch4        ch3        ch2
ch2(s)     c          ch         c2h6       c2h5
c2h4       c2h3       c2h2       c2h        ch3cho
ch3co      ch2cho     ch2co      hcco       hccoh
ch3co3h    ch3co3     ch3co2     c2h5oh     c2h5o
pc2h4oh    sc2h4oh    o2c2h4oh   c2h5o2h    c2h5o2
```

```
c2h4o2h      c2h4o1-2      c2h3o1-2      ch3coch3      ch3coch2
ch3coch2o2                                c2h3cho       c2h3co !wkm 22/02/2010 ch3coch2o2h, ch3coch2o
removed
c2h5cho      c2h5co        ch3och3       ch3och2       ch3och2o2
ch2och2o2h   ch3och2o2h    ch3och2o      o2ch2och2o2h  ho2ch2ocho
och2ocho     hoch2oco      ch3ocho       ch3oco        ch2ocho
he           c3h8          ic3h7         nc3h7         c3h6
c3h5-a       c3h5-s        c3h5-t        c3h4-p        c3h4-a
c3h3         c3h2          c3h5o         c3h6ooh1-2    c3h6ooh1-3
c3h6ooh2-1   c3h6ooh1-2o2   c3h6ooh1-3o2  c3h6ooh2-1o2  c3h6ooh2-2
nc3h7o2h     ic3h7o2h      nc3h7o2       ic3h7o2       nc3h7o
ic3h7o       c3h6o1-2      c3h6o1-3      c3ket12       c3ket13
c3ket21      c3h51-2,3ooh  c3h52-1,3ooh  c3h6oh        hoc3h6o2
ch3chco      ac3h5ooh      c2h3ooh
end
reactions

!wkm 27/07/2010
!from stanford
!ref:hessler, j. phys. chem. a, 102:4517 (1998)
!h+o2<=>o+oh 3.547e+15 -0.406 1.660e+04
h+o2<=>o+oh 1.04+14 0.0 1.5286e+04

!ref:sutherland et al., 21st symposium, p. 929 (1986)
o+h2<=>h+oh 5.080e+04 2.670 6.292e+03

!ref:michael and sutherland, j. phys. chem. 92:3853 (1988)
oh+h2<=>h+h2o 2.160e+08 1.510 3.430e+03

!ref:sutherland et al., 23rd symposium, p. 51 (1990)
o+h2o<=>oh+oh 2.970e+06 2.020 1.340e+04

!ref:tsang and hampson, j. phys. chem. ref. data, 15:1087 (1986)
h2+m<=>h+h+m 4.577e+19 -1.400 1.044e+05
h2/2.5/ h2o/12/ co/1.9/ co2/3.8/
o+o+m<=>o2+m 6.165e+15 -0.500 0.000e+00
h2/2.5/ h2o/12/ ar/.83/ co/1.9/ co2/3.8/ ch4/2/ c2h6/3/ he/.83/
o+h+m<=>oh+m 4.714e+18 -1.000 0.000e+00
h2/2.5/ h2o/12/ ar/.75/ co/1.5/ co2/2/ ch4/2/ c2h6/3/ he/.75/
h+oh+m<=>h2o+m 4.500e+22 -2.000 0.000e+00
h2/.73/ h2o/12/ ar/.38/ ch4/2/ c2h6/3/ he/.38/

!ref:cobos et al., j. phys. chem. 89:342 (1985) for kinf
h+o2(+m)<=>ho2(+m) 1.475e+12 0.600 0.000e+00
!HENRY:Ref for low pressure limit??
low / 3.4820e+16 -4.1100e-01 -1.1150e+03 /
troe / 5.0000e-01 1.0000e-30 1.0000e+30 1.0000e+10 / !troe fall-off reaction
h2/1.3/ h2o/14/ ar/.67/ co/1.9/ co2/3.8/ ch4/2/ c2h6/3/ he/.67/

!ref:tsang and hampson, j. phys. chem. ref. data, 15:1087 (1986) [modified]
ho2+h<=>h2+o2 1.660e+13 0.000 8.230e+02
ho2+h<=>oh+oh 7.079e+13 0.000 2.950e+02
```

```
!ref:baulch et al., j. phys. chem. ref data, 21:411 (1992)
ho2+o<=>oh+o2 3.250e+13 0.000 0.000e+00

!wkm 27/07/2010
!from stanford
!same
!ref:keyser, j. phys. chem. 92:1193 (1988)
ho2+oh<=>h2o+o2 2.890e+13 0.000 -4.970e+02

!ref:hippler et al., j. chem. phys. 93:1755 (1990)
ho2+ho2<=>h2o2+o2 1.030e+14 0.000 1.104e+04
dup

!ref:Kappel et al., pccp. 4 (2002) 4392-4398
ho2+ho2<=>h2o2+o2 1.940e+11 0.000 -1.409e+03
dup

!wkm 27/07/2010
!from stanford
!ref:brouwer et al., j. chem. phys. 86:6171 (1987) for kinf
!ref:warnatz, j. in combustion chemistry (1984) for k0
!h2o2(+m)<=>oh+oh(+m) 2.951e+14 0.000 4.843e+04
!low / 1.2020e+17 0.0000e+00 4.5500e+04 /
!troe / 5.0000e-01 1.0000e-30 1.0000e+30 1.0000e+10 / !troe fall-off reaction
!h2/2.5/ h2o/12/ ar/.64/ co/1.9/ co2/3.8/ ch4/2/ c2h6/3/ he/.64/
h2o2(+m)<=>oh+oh(+m) 8.59e+14 0.000 4.856e+04
low / 9.55e+15 0.0000e+00 4.2203e+04 /
troe / 1.0 1e+30 1e+30 / !troe fall-off reaction
n2/1.5/ h2o/9.0/
```

VITA

William Baugh Lowry received his Bachelor of Science degree in mechanical engineering from Texas A&M University in 2008. He then entered the graduate program at Texas A&M University and received his Master of Science degree in mechanical engineering in December of 2010. During his graduate work, Lowry authored 3 journal publications and 4 conference papers. He also gave presentations at 4 national and international conferences and symposia. His interests include experimental design, gas dynamics, and general combustion research.

Mr. Lowry may be reached at the Department of Mechanical Engineering, 3123 TAMU, Texas A&M University, College Station, TX 77843-3123. His email is willlowry@neo.tamu.edu